Hindawi
Advances in Civil Engineering
Volume 2022, Article ID 2121214, 24 pages
https://doi.org/10.1155/2022/2121214

Research Article

Resilient Performance of Self-Centering Hybrid Rocking Columns: Theory, Experiment, and Numerical Simulation

Shi Yan,[1] **Tao Wang**,[1,2] **and Xing Su**[1]

[1]*School of Civil Engineering, Shenyang Jianzhu University, Shenyang 110168, China*
[2]*Qingdao Country Garden Bolin Real Estate Co Ltd, Qingdao 266100, China*

Correspondence should be addressed to Tao Wang; wangtao@stu.sjzu.edu.cn

Received 7 May 2022; Accepted 2 September 2022; Published 11 October 2022

Academic Editor: Iman Mansouri

A novel self-centering hybrid rocking column (HRC) with a replaceable soft steel energy dissipator (RED) is proposed to solve the issue of traditional frame structures being vulnerable to damage during earthquakes and difficult rehabilitation after. The resilient performance of the proposed RED-HRC was investigated by using theoretical, experimental, and numerical methods. The yield states of the designed RED are taken as the control points to establish theoretically the corresponding relationship $f(M, \theta)$ between the overturning moment M and the rotation angle θ of the RED-HRC. In addition, a group of RED-HRC specimens were tested under pseudo static loading to investigate the resilient performance by considering the main influencing factors of the cross-sectional area of the prestressed unbonded tendons, the initial value of the prestressing force, the axial compression ratio of HRCs, and the thickness of the RED. Moreover, a finite element model (FEM) validated by the experimental data was established by using the ABAQUS platform to further study the resilience of the proposed RED-HRCs, focusing on the energy dissipating efficiency of the RED. The design method and process for the RED-HRC were finally developed. A typical hysteretic response with "double-flag shape" characteristics was obtained. These results show that the proposed RED-HRC has excellent resilient performances of good energy dissipation capacity, strong self-centering ability, and high strength and stiffness, realizing the goal of low damage level during the earthquake and quick rehabilitation after.

1. Introduction

Earthquakes, as a kind of destructive natural disaster, may endanger human safety and the social economy. Structures should ensure necessary functionality to prevent them from being damaged or even collapsed during earthquakes through proper design methods. Traditional building structures usually adopt ductile design methods to achieve the goal of dissipating seismic energy by allowing structural members to plastically deform. However, due to the complexity and uncertainty of earthquakes, some structural components might be damaged during earthquakes and undoubtedly difficult to be retrofitted after. Besides, the cost of rehabilitation might be too high to afford due to the excessive plastic deformation at failure locations. Therefore, it is of great significance to solve the problem and achieve innovative earthquake resilient structures (ERSs), which are distinguished from the traditional ones.

The novel ERS [1, 2] means that the structure can quickly recover its function without repair or minor repair in minor earthquakes or major ones. At present, the forms of ERS may mainly include rocking structures [3], self-centering structures [4], replaceable component structures [5], and self-centering hybrid structures [6]. Among them, rocking structures mainly including rocking frame (RF) structures [7–9] and –frame-rocking wall (FRW) structures [10–12], as well as bridge structures with rocking piers [13–15], are focused due to the excellent resilient capacity. Housner [16] first proposed the concept of rocking structures and a classical rocking rigid-body model and proved that the structures have excellent seismic performance. Roh [17–20] further proposed the concept of a rocking column for the first time to reduce the component constraints and seismic acceleration response. In January 2009, at the NEES/E-Defense US-Japan Earthquake Engineering Phase 2 Cooperative Research Program Conference, scholars from the

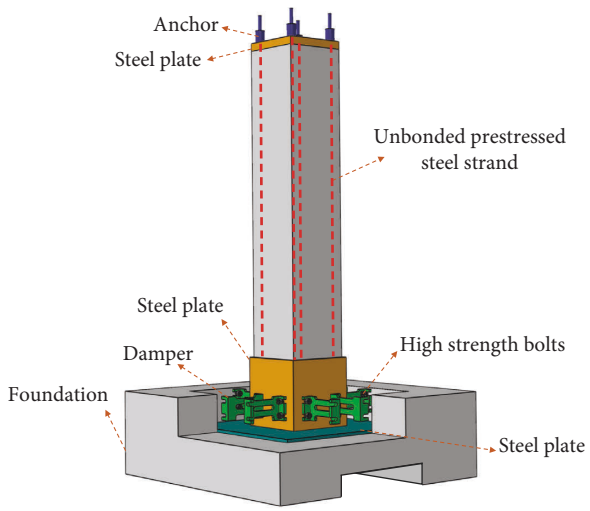

Figure 1: The schematic in detail of the RED-HRC joint with RC foundation.

United States and Japan proposed that "resilient city" should be taken as the general direction of earthquake engineering cooperation for the first time [21]. Since then, the importance of "recoverable function" has been further emphasized in the annual meeting of the Pacific Earthquake Engineering Research Center (PEER) [22] and the 16th World Earthquake Congress [23]. The ERS has become the focus of earthquake engineering research.

In the system of ERS, four kinds of typical working mechanisms including the rocking mechanism, self-centering mechanism, replaceable member mechanism, and centralized energy dissipation mechanism are summarized in general [24]. In a hybrid system of self-centering rocking structures, the combination of two or more working mechanisms is usually adopted, and many kinds of component connection forms have been proposed [25–34]. However, among them, the connections with higher energy dissipation capacity usually have the problem of lower self-centering ability, or the connections with better self-centering capacity might have a weaker energy dissipation ability. How to solve the problem and enhance the earthquake resilient performance (ERP) become urgent, therefore, it is necessary to propose a new type of rocking structure, e.g., the self-centering hybrid rocking column (HRC), in which bondless prestressed tendons are placed to provide self-centering forces, with external replaceable soft steel energy dissipators (RED). The proposed RED-HRC has the advantage of higher energy dissipation, stronger self-centering capability, and moderate lateral stiffness than the conventional one, meeting the functional requirements of rocking structures.

To study the mechanism and ERP of the RED-HRC, a rigid-body hysteresis model of HRC was proposed, and the equations describing the relationship between overturning moment M and rotation angle θ were established and theoretically solved. Meanwhile, to verify the excellent self-centering performance of the proposed HRC, a group of pseudo static tests under 7 different working cases were performed, considering the influences of the cross-sectional area of prestressed tendons, the initial value of prestressing force, the axial compression ratio of HRCs, and the thickness of REDs. A proposed RED-HRC finite element model was also established based on the ABAQUS platform. After the model was verified, the influences of each parameter on self-centering performance were systematically studied. Finally, the rocking process of the HRC is simplified, and the design process was summarized from the elastic stage to the elastoplastic one. The results show that the proposed RED-HRC has a typical "double-flag shape" hysteretic response, reflecting excellent seismic resilient functionality.

2. Mechanism of RED-HRC

The goal of the innovative RED-HRC is to release restraints at column bottom connections to prevent damages during earthquakes, resulting in the column's rocking deformation in a certain range. The change of the structural form may alter the working mechanisms for which new requirements will be put forward. The schematic in detail of the RED-HRC joint with the foundation is shown in Figure 1. The rocking column made of precast reinforced concrete (RC) in which a group of unbounded prestressed tendons are embedded is connected to an RC foundation through a number of REDs and prestressed tendons. Two steel plates for protecting concrete are pre-embedded in the HRC and foundation, respectively, forming a contact rocking surface, and preventing the local concrete from crushing and other damages during the "rocking" process of the RED-HRC. Prestressing forces applied by posttensioned unbounded prestressed tendons can provide efficient self-centering forces for the RED-HRC, and the prestressed tendons should keep in an elastic state during major earthquakes through a predesign method. The working mechanisms of the RED-HRC will be based on the following aspects:

For damping mechanisms, traditional RC columns dissipate seismic energy through concrete cracking and slippage between steel bars and concrete, resulting in a relatively weak energy dissipation capacity. However, the optimally designed REDs can significantly improve the energy dissipation capacity. Since the REDs are connected to the HRC and RC foundation through embedded bolts which are specially designed to ensure undamaged during the "rocking" process, the HRC bottom is allowed to lift and rock around the rocking surface. The concentrated deformation due to rocking makes the REDs, which are installed in special locations, sufficiently working to provide enough damping effects on the seismic energy dissipation and structural response reduction. Although the REDs might be damaged during major earthquakes, their replaceable performance is interested in by civil engineers.

For replaceable member mechanisms, the RED-HRC member mainly concentrates seismic energy on the REDs, while the corresponding main structure shares a small amount to achieve the purpose of damage concentration, controllability, and protection of the main structure. The RED can be designed to realize the purpose of keeping in an elastic state during minor (or moderate) earthquakes and in the elastoplastic state to dissipate seismic energy during

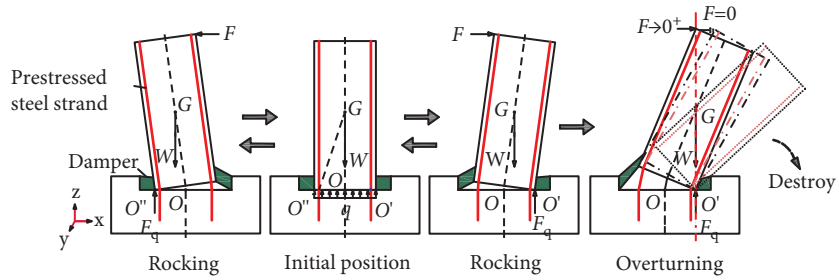

Figure 2: The schematics of the rocking process for the RED-HRC.

moderate (or major) earthquakes. Moreover, the damaged RED can be rapidly removed and reinstalled after the earthquake to accomplish the resilient function.

For rocking mechanisms, the schematic of RED-HRC's rocking process is shown in Figure 2. The stress distribution on the column bottom contact surface is changing during the rocking process. In the initial state, the contact stress is evenly distributed. After a horizontal action such as an earthquake ground motion is applied, the compressive stress on the contact surface on the tension side begins to decrease and gradually tends to 0, and the compressive stress on the compression side gradually increases. As the horizontal load gradually increases, the column bottom contact stress begins to decrease, and the contact stress concentrates on the compression side. When the entire contact surface reaches the ultimate state, which is defined as rebars passing through the surface yielded, the maximum bending moment M_{max} at the column bottom is defined, and the RED-HRC reaches the rocking critical state. As continuing to increase the horizontal load, the RED-HRC will have the rocking behavior and still maintains a certain anti-overturning ability. When the gravitational action line passes through the support point, the RED-HRC reaches the critical overturning state [35]. Once the deformation exceeds this state, the structure will overturn and fail. Therefore, the key points are getting hold of both allowing the RED-HRC to rock in a certain range during minor (or moderate) earthquakes and preventing it from overturning during major earthquakes by limiting the ultimate rotation angle.

For self-centering mechanisms, both prestressed tendons and the gravity of the RED-HRC can sufficiently provide elastic restoring forces to make it automatically move back to the central position. The important self-centering performance is the key issue to realize the resilient functionality of the RED-HRC. The higher prestressing forces coming from both higher prestressing levels and greater prestressed tendon cross-sectional areas are beneficial for the more sufficient self-centering performance. In addition, the self-centering capacity of HRC is associated with the dissipation ability of REDs because the damping force might restrict the self-centering performance. Therefore, the reasonable selection for the self-centering and energy dissipation capacities of the RED-HRC is helpful to improve the resilient functionality.

The proposed RED-HRC can reflect the characteristics of ERPs to achieve the goal of ERS based on the mechanisms of high damping, targeted replaceable REDs, suitable rocking behavior, and powerful self-centering ability during earthquakes.

3. Theoretical Analysis on Hysteretic Performance

3.1. Basic Assumptions. In this paper, a typical HRC is selected as the research objective to theoretically analyze the hysteretic performance under horizontal pseudo-static loading. A simplified theoretical model is established, and 11 key control points are applied to describe the characteristics of hysteretic performance with several main influencing factors during the "rocking" process. Therefore, the following basic assumptions are made for the hysteretic model of RED-HRC to simplify the theoretical analysis.

(1) The "rocking" column is regarded as a rigid body. Therefore, during the "rocking" process, the contact surfaces have only two working cases: fully contacted (closed) and single point (point of rotation) contacted (opened). Meanwhile, the self-deformation of the "rocking" column is neglected due to the rigid-body assumption, i.e., the influences of longitudinal reinforcement deformation, concrete cracking and crushing, etc., are not considered on the geometric size of members, energy dissipation capacity, and self-centering performance.

(2) The influences of bending and shear deformation of the "rocking" column are not considered, and the "rocking" column is regarded as a rigid body rotation around the point of rotation.

(3) The prestressed tendons providing elastic restoring forces in the HRC will be in a linear elastic state. Therefore, a linear constitutive law is selected for the prestressed tendons.

(4) The material of RED will be in an ideal elastic-plastic state. Therefore, an elastic-plastic model for the corresponding constitutive law is selected.

(5) No slippage will occur between the contact surfaces. The surfaces between the rigid "rocking" column and foundation can be opened or closed but no slippage.

Based on the above basic assumptions, the schematic of the typical RED-HRC "rocking" process is shown in Figure 2, including the initial state, the rocking state, and the overturning state. The corresponding relationship between the overturning moment M and rotation angle θ is shown in Figure 3.

The typical hysteretic curve between M and θ is conceptually like a "double-flag" with 11 key control points,

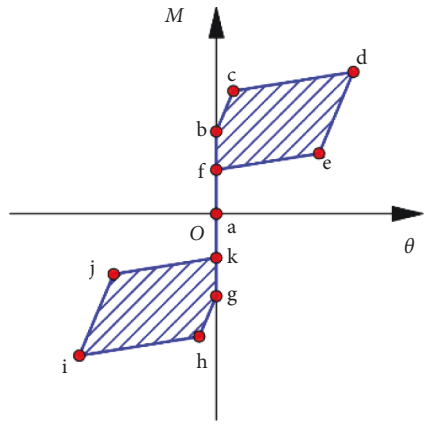

Figure 3: Typical hysteretic relation curve between overturning moment (M) and rotation angle θ.

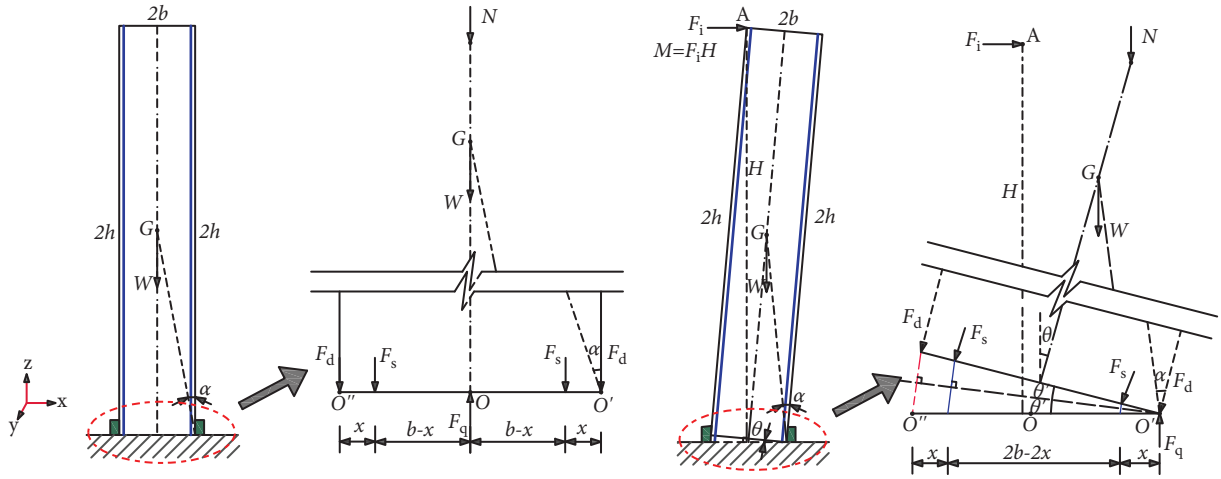

Note: Non-proportional magnification.

(a) (b)

Figure 4: The schematics of the RED-HRC forces and deformations. (a) In the initial state. (b) In the rocking state.

named the "double-flag shape" curve, reflecting the ideal resilient performance of the RED-HRC due to the characteristics of no residual rotation ("a" point), good energy dissipation capacity (shaded area), high yield moment ("c" or "gg" point), and high bearing ability and sufficient ductility ("d" or "i" point). Therefore, each segment between two adjacent points is assumed as a linear one.

3.2. Establishment of Resilience Model. The schematics of RED - HRC forces and deformations are shown in Figure 4. The rigid body of RED- HRC selected as a free body is used as the analysis objective to set up equations of static equilibrium. Since the height of HRC is much larger than its width ($2h >> 2b$), the angles of α and θ are relatively small. Here, F_d denotes the resultant force provided by the RED at one side of the contact surface. We assume that F_d is perpendicular to the HRC bottom surface due to the small θ. According to the force state, three equations of static equilibrium are set up as follows:

$$\sum F_x = 0, \sum F_z = 0, \text{and} \sum M = 0, \tag{1}$$

where ΣF_x and ΣF_y represent resultant forces along x andz directions, respectively, and ΣM denotes the resultant moment at any support point, as shown in Figure 4. The clockwise direction of the overturning moment M is defined as positive, and the anticlockwise one as negative. Based on (1), the relationship between the corresponding overturning moment M and rotation angle θ can be established according to the following cases, respectively.

(1) In the initial state (for the case at point "a")

In this case, the HRC is not affected by the horizontal load. Therefore, the coordinates of "a" point can be calculated, that is,

$$M = 0, \theta = 0. \tag{2}$$

(2) Compression critical state at "positive direction" (for the case at point "b")

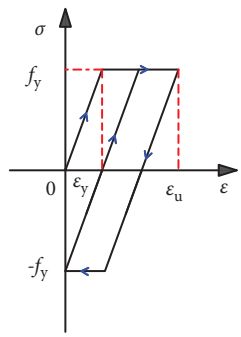

Figure 5: The constitutive relationship of RED material.

The coordinates of the "b" point are calculated as follows:

$$M = Wb + 2\sigma_{s0}A_p b + N, b\theta = 0, \tag{3}$$

where σ_{s0} is the initial stress of prestressing tendons, N is the vertical axial load, W is the gravity of the HRC, h and b are the half-height and the half-width of the HRC, respectively, andA_p is the cross-sectional area of prestressing tendon, respectively.

(3) RED yield state at "positive direction" (for the case at point "c")

The coordinates of the "c" point is calculated as follows:

$$\begin{aligned} M &= F_i(2b\sin\theta + 2h\cos\theta) \\ &= 2F_{d1}b + \left[\sigma_{s0}A_p + \frac{2(2b-x)\sin\theta'}{l_s}E_pA_p\right](2b-x) \\ &\quad + \left[\sigma_{s0}A_p + \frac{2x\sin\theta'}{l_s}E_pA_p\right]x + W(b\cos\theta - h\sin\theta) \\ &\quad + N(b\cos\theta - 2h\sin\theta) + M_i' + M_i'', \\ \theta &= 2\arcsin\frac{\varepsilon L}{2b}, \end{aligned} \tag{4}$$

where F_i is the horizontal load, θ' is the half of rotation angle, $\theta = 2\theta'$, α is the angle between the HRC gravity line and line segment GO$'$, and Fd_1 is the RED yield force along the z direction. Since the REDs along the x-direction are not yielded simultaneously, therefore, F_d can be obtained according to a pushover analysis. The yield point is determined through the "energy method." Fd_i is the force corresponding to different periods of the energy dissipator obtained by the pushover analysis, $M' = F_{di} \cdot L$, $M' = M''$, where $i = 1, 2, 3...$ and L is the effective length of RED, x is the horizontal distance between prestressed tendon and HRC sideline, l_s is the effective length of prestressing tendon, and ε is strain. The material constitutive relationship of RED is shown in Figure 5.

(4) Critical overturning state at "positive direction" (for the case at point "d")

As shown in Figure 2, due to the angle α of the HRC being relatively small, when the rotation angle θ is equal to α, the REDs and the prestressed tendons can still provide part of the anti-overturning moment. As F continues being applied, the rotation angle θ of RED-HRC is greater than α, the REDs and the prestressed tendons begin to partially fail. When F is equal to 0, the material defects of the REDs and the prestressed tendon should be considered. Meanwhile, the RED-HRC will overturn. Considering the safety, $\theta = \alpha$ is set as the critical point, and the anti-overturning factor δ $(0 < \delta < 1)$ is introduced, therefore, $\theta = \delta\alpha$ and δ can be determined in advance according to the safety requirements. Therefore, the coordinates of the "d" point can be calculated as follows:

$$\begin{aligned} M &= F_i(2b\sin\delta\alpha + 2h\cos\delta\alpha) \\ &= 2F\mathrm{d}_2 b + \left[\sigma_{s0}A_p + \frac{2(2b-x)\sin(\delta\alpha/2)}{l_s}E_pA_p\right](2b-x) \\ &\quad + \left[\sigma_{s0}A_p + \frac{2x\sin(\delta\alpha/2)}{l_s}E_pA_p\right]x \\ &\quad \pm N(b\cos\delta\alpha - 2h\sin\delta\alpha) + M_i' + M_i'', \\ \theta &= \delta\alpha \end{aligned} \tag{5}$$

(5) RED unloading yield state at "positive direction" (for the case at point "e")

Considering the influence of concrete damage, the RED and prestressed tendon material defects on the self-centering effect of RED-HRC in practical engineering and two stiffness reduction coefficients ς and κ $(\varsigma < 1, \kappa < 1)$ are introduced, representing the stiffness reduction coefficients of REDs and prestressed tendons, respectively. The coordinates of the "e" point are calculated as follows:

$$M = F_i(2b\sin\theta + 2h\cos\theta)$$

$$= -2F_{d3}b + \left[\sigma_{s0}A_p + \frac{2(2b-x)\sin\theta'}{l_s}E_pA_p\right](2b-x)$$

$$+ \left[\sigma_{s0}A_p + \frac{2x\sin\theta'}{l_s}E_pA_p\right]x + W(b\cos\theta - h\sin\theta)$$

$$+ N(b\cos\theta - 2h\sin\theta) + M_i' + M_i'',$$

$$\theta = 2\arcsin\left(\frac{2b\sin\theta' - 2l_e\varepsilon}{2b}\right). \tag{6}$$

(6) Returning back to the original position at "positive direction" (for the case at point "f")

The coordinates of the "f" point are calculated as follows:

$$M = Wb + 2\sigma_{s0}A_pb + Nb - 2F_{d4}b - M_i'' - M_i'', \theta = 0. \tag{7}$$

(7) Compression critical state at "negative direction" (for the case at point "gg")

Similarly, the coordinates of "gg" point are calculated as follows:

$$M = -\left(Wb + 2\sigma_{s0}A_pb + Nb - 2F_db - M_i' - M_i''\right), \theta = 0. \tag{8}$$

When the RED-HRC is reset in the forward direction, the REDs are still in the reverse yield state.

(8) RED yield state at "negative direction" (for the case at point "h")

$$M = F_i(2b\sin\theta + 2h\cos\theta) = -\left\{2F_{d5}b + \left[\sigma_{s0}A_p + \frac{2(2b-x)\sin\theta'}{l_s}E_pA_p\right](2b-x)\right.$$

$$\left. + \left[\sigma_{s0}A_p + \frac{2x\sin\theta'}{l_s}E_pA_p\right]x + W(b\cos\theta - h\sin\theta) + N(b\cos\theta - 2h\sin\theta) + M_i' + M_i''\right\}, \tag{9}$$

$$\theta = 2\arcsin\frac{\varepsilon L}{2b}.$$

(9) Critical overturning state at "negative direction" (for the case at point "i")

$$M = F_i(2b\sin\delta\alpha + 2h\cos\delta\alpha) = -\left\{2F_{d6}b + \left[\sigma_{s0}A_p + \frac{2(2b-x)\sin\delta\alpha/2}{l_s}E_pA_p\right](2b-x)\right.$$

$$\left. + \left[\sigma_{s_0}A_p + \frac{2x\sin\delta\alpha/2}{l_s}E_pA_p\right]x \pm N(b\cos\delta\alpha - 2h\sin\delta\alpha) + M_i' + M_i''\right\}, \theta = \delta\alpha. \tag{10}$$

(10) RED unloading yield state at "negative direction" (for the case at point "i")

$$M = F_i(2b\sin\theta + 2h\cos\theta) = -\left\{-2F_{d7}b + \left[\sigma_{s0}A_p + \frac{2(2b-x)\sin\theta'}{l_s}E_pA_p\right](2b-x)\right.$$

$$\left. + \left[\sigma_{s0}A_p + \frac{2x\sin\theta'}{l_s}E_pA_p\right]x + W(b\cos\theta - h\sin\theta) + N(b\cos\theta - 2h\sin\theta) + M_i' + M_i''\right\}, \quad (11)$$

$$\theta = 2\arcsin\left(\frac{2b\sin\theta' - 2l_e\varepsilon}{2b}\right),$$

(11) Returning back to the original position at "negative direction" (for the case at point "k")

$$M = -\left[Wb + 2\sigma_{s0}A_pb + Nb - 2F_{d4}b - M_i' - M_i''\right], \theta = 0. \quad (12)$$

In summary, during the "rocking" process of the RED-HRC, the differences between "positive direction" and "negative direction" are focused on the initial cases. The initial stress state of REDs in the "positive direction" is 0, but the initial stress state of REDs in the "negative direction" has residual stress.

3.3. Theoretical Hysteretic Model Verification and Analysis. Both a finite element model (FEM) and an experiment result were used to verify the accuracy of the proposed theoretical hysteretic model. The experimental result of a new recoverable rocking column completed by Liu et al. [32] was selected for the comparison. Meanwhile, the experimental working condition S16-5.5-0.1-AR performed by the author of this paper was also selected for model verification.

For the comparison, three kinds of data of experimental, FEM, and theoretical ones were calculated, respectively, based on parameters in reference [32] in which a hysteresis loop corresponding to the peak rotation angle of 5% was selected as the comparison one. According to the data in the selected experimental loop, the theoretical and FEM-based hysteresis loops were calculated, and corresponding curves were drawn, focusing on the data in the 11 theoretical cases, shown in Figure 3. The comparison results are shown in Figure 6.

From Figure 6, the three kinds of results for the working case S16-5.5-0.1-AR are generally in good agreement, and this can validate the efficiency and correctness of the proposed theoretical hysteretic model. However, there are also relatively small errors among the three results. After the error analysis, the main reasons for the errors are including the following:

(1) In the loading stage, the theoretical hysteretic model shows obvious three-stage linear segments, while the finite element analysis and test results have no obvious sudden change in stiffness, which is related to the assumption of the rigid rocking body in the theoretical model.

(2) In the third stage of loading, the stiffness and ultimate anti-overturning moment in the theoretical model are slightly lower than those of the finite element analysis and test results. The main reason may be that the stress-strain relationship of steel in the theoretical model obeys an ideal elastic-plastic law, and the reinforcement hardening effects after the yield point are not considered.

(3) When unloading, the corresponding residual deformation in the theoretical model is slightly smaller than that of the finite element analysis and test results, which is mainly related to ignoring the HRC concrete cracking and nonlinear interfacial slippage in the theoretical analysis.

In addition, since the prestressing forces in the three kinds of cases are not high enough to provide sufficient self-centering ability, the hysteresis curves do not reflect the typical "double-flag shape" and remain an obvious residual rotation angle when the overturning moment becomes zero. Therefore, the area of prestressed tendons and prestressing force level should be great enough to ensure the self-centering capacity if a very small resilient performance of the RED-HRC is required.

4. Experimental Validation on Resilient Performance

4.1. Specimen Design. The goal of the experiment is to validate both the resilient performances of the proposed RED-HRC under pseudo-static loading and the efficiency of the proposed theoretical hysteretic model. Therefore, the specimen design was carried out according to the "specification" [36] in China. The concrete grade of members is C30, the longitudinal steel bars are HRB335, the other steel bars are HPB300, and the thickness of the concrete cover is 20 mm. The sectional dimension of the concrete rocking column is 400 mm × 400 mm, the height of the rocking column is 1800 mm, the longitudinal reinforcements are 12Φ16, the stirrup is Φ8@100, and the shear-span ratio is 4. The sectional dimension of the concrete foundation is 1670 mm × 1670 mm, and the height is 900 mm. A group of connecting bolts is pre-embedded in the precast RC rocking column and the

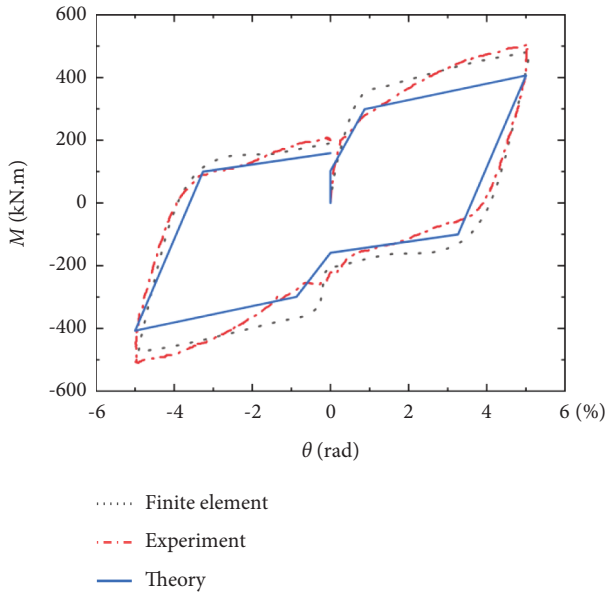

Figure 6: The comparison of experimental, theoretical, and FEM results.

foundation, respectively, for the connection of REDs. The steel plates for protecting concrete are also pre-embedded on the surface of the foundation, the four sides, and two end surfaces of the HRCs, respectively. Four longitudinal channels for the construction of posttensioned unbonded prestressed tendons are reserved as casting concrete, and the prestress is applied in the posttensioned unbonded prestressed tendons before testing. The specific specimen dimension and reinforcement in detail are shown in Figure 7.

4.2. Material Tests. Concrete standard test blocks and various standard rebar drawing test pieces were tested on the material property testing machine of the Structural Laboratory of Shenyang Jianzhu University. The results are shown in Tables 1–4.

4.3. Experimental Program. The pseudo-static loading tests were carried out with the MTS-produced hydraulic servo actuator in the Structural Engineering Laboratory of Shenyang Jianzhu University. An axial load was vertically applied through a 1000 kN hydraulic Jack, and a 500 kN actuator produced by MTS Company was used to apply a horizontal pseudo-static load to the RED-HRC specimens. The loading scheme and schematic of the pseudo-static loading test are shown in Figures 8 and 9, respectively. The horizontal displacement at the top of the RED-HRC was controlled by the displacement/rotation angle. Before the RED-HRC started rocking, the force-controlled loading scheme was carried out for the first cycle; when the RED-HRC started rocking, the displacement-controlled loading scheme was performed, and two cycles were performed for each loading step. The test was terminated immediately when one of the following conditions occurs:

(1) The specimen reaches the design drift angle (1/25)
(2) The REDs fail from the working state
(3) The prestressed tendon reaches the "yield" state
(4) The horizontal load drops below 85% of the maximum horizontal load

In addition, a self-carrying measuring system produced by MTS company was used to measure the displacement at the top of the RED-HRC; meanwhile, 8 displacement gauges were arranged at the given positions of the RED-HRC surface to measure the actual displacements, shown in Figure 9. Moreover, four 1000 kN perforated load sensors were installed in each prestressing tendon at the top of the RED-HRC specimen to measure prestressing force changes of prestressed tendons. The measurement started by applying the initial prestressing force for prestressed tendons. The experimental layout is shown in Figure 10.

The test case design and loading scheme are shown in Table 5 in which 7 working cases were set up in the test according to different influencing factors of the thickness of RED, the initial value of the prestressed tendons, the axial compression ratios, the cross-sectional areas of prestressed tendon, and so on. The specimens from Specimen 1 to Specimen 6 are designed as the RED-HRCs, and Specimen 7 is designed for the ordinary rocking column (ORC) with REDs, named RED-ORC. The name format of specimens in each test case is "ZX (number)-XX (axial compression ratio)-XX (initial prestress value)-XX (thickness of RED)." For example, the case of "Z1-0.1-0.4-10" means the column number of Z1, the axial compression ratio of 0.1, the initial value of prestress of 0.4 f_u, and the thickness of RED of 10 mm.

5. Experimental Process and Result Analysis

5.1. Experimental Phenomena. The experimental phenomena for the seven specimens have typical and similar characteristics in terms of resilient performances. Due to the limitation of paper space, Specimen 1 (Z1-0.1-0.4-10) is taken as an example to analyze experimental phenomena during or after the loading process. For other specimens, see reference [37]. For Specimen 1, Figures 11 and 12 are the deformation and the failure of RED during and after testing, respectively, corresponding to maximum rocking position with the rotation angle of 1/25, which is the limit of structural rotation angle under extremely major earthquakes recommended by the China code. Under joint actions of elastic restoring forces provided by prestressed tendons and elastoplastic forces from REDs, the hysteresis curve for Specimen 1 displays the characteristic of "double-flag shape" hysteretic response, shown in Figure 13(a), which verifies the excellent resilient ability of the proposed RED-HRCs.

During the pseudo-static loading process, when the peak displacement of a cycle at the top of Specimen 1 (simplified as the peak displacement) reached 13 mm, the uplift at the HRC bottom can be observed, and the initial state of rocking can be reached, as shown in Figure 11(a). When the peak displacement reached 23 mm, a slight noise was produced between the REDs and the HRC, indicating the RED started

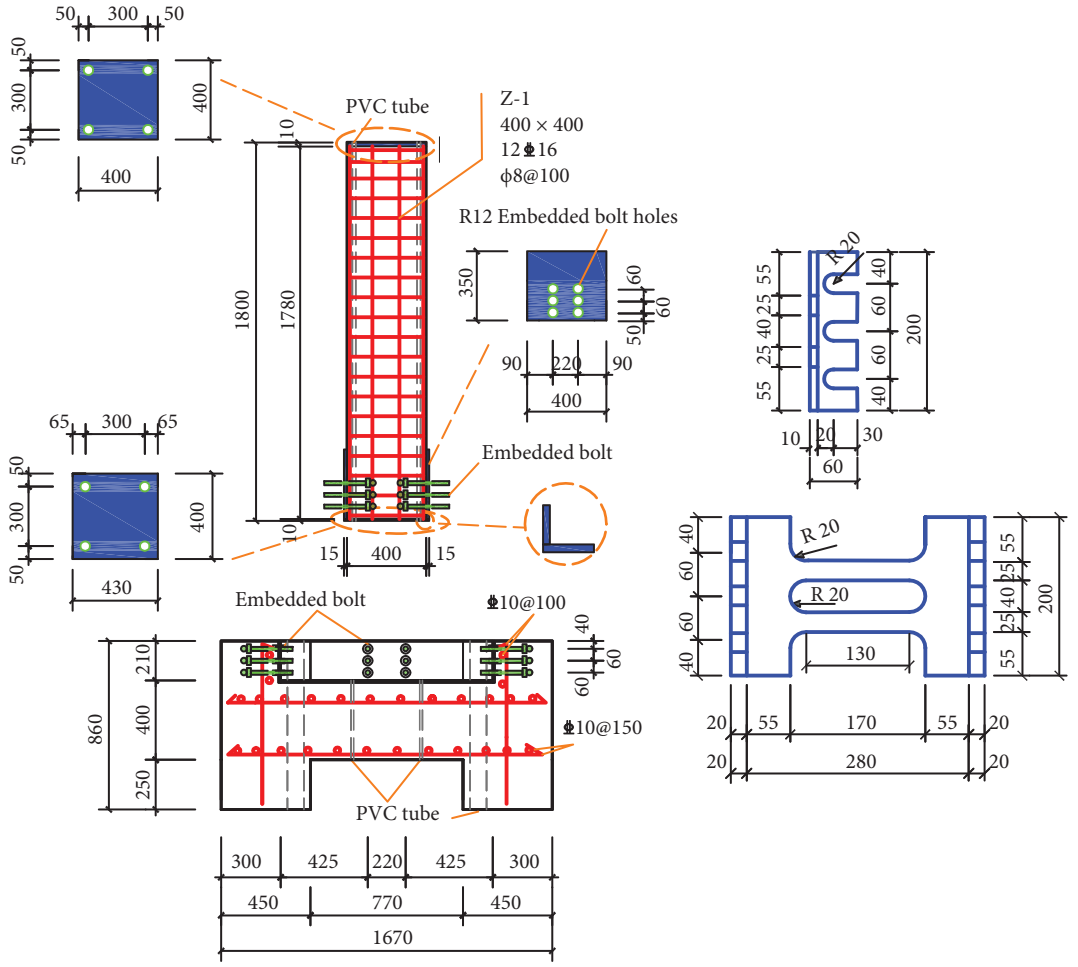

Figure 7: Construction drawing in detail of the RED-HRC (unit: mm). (a) Reinforcement and dimension of RED-HRC. (b) Dimension of RED.

Table 1: Performance test results of rebars.

Rebar diameter (mm)	Design strength (MPa)	The measured value of yield strength (MPa)	Mean value (MPa)	The measured value of ultimate strength (MPa)	Mean value (MPa)	Modulus of elasticity (MPa)
16	300	361.95 346.41 348.68	352.35	504.51 488.40 490.82	494.57	200000

Table 2: Performance test results of prestressing tendons.

Tendon diameter (mm)	The measured value of yield-bearing capacity (kN)	Mean value (kN)	The measured value of ultimate bearing capacity (kN)	Mean value (kN)	Modulus of elasticity (MPa)
12.7	170.58 171.73 170.85	171.05	188.84 188.41 187.96	188.40	200000
15.2	244.79 239.40 236.80	240.33	272.39 270.37 270.43	271.06	

to yield. Meanwhile, neither the REDs nor the HRC was obviously deformed or cracked. When the peak displacement reached 38 mm, the REDs deformed significantly, and the HRC itself did not have any cracks or self-deformation, just observing a rotation of the rigid body, as shown in Figures 11(b) and 11(c). When the peak displacement

Table 3: Performance test results of concrete.

Strength grade	The measured value of compressive strength (MPa)	Mean value (MPa)
C30	36.23 28.90 31.16	32.10

Table 4: Performance test results of steel plates.

Type of steel and thickness	Modulus of elasticity (GPa)		Yield strength (MPa)		Ultimate strength (MPa)	
	Measured	Mean	Measured	Mean	Measured	Mean
Q235 (6 mm)	224.17 186.87	205.52	307.02 336.06	321.54	408.15 449.07	428.61
Q235 (10 mm)	179.71 201.65	190.68	318.95 308.72	313.84	452.35 446.51	449.43
Q235 (14 mm)	196.32 172.77	184.54	346.68 352.61	349.65	503.73 508.22	505.98
Q345 (10 mm)	249.65 222.64	236.14	412.03 408.78	410.41	491.93 487.54	489.74

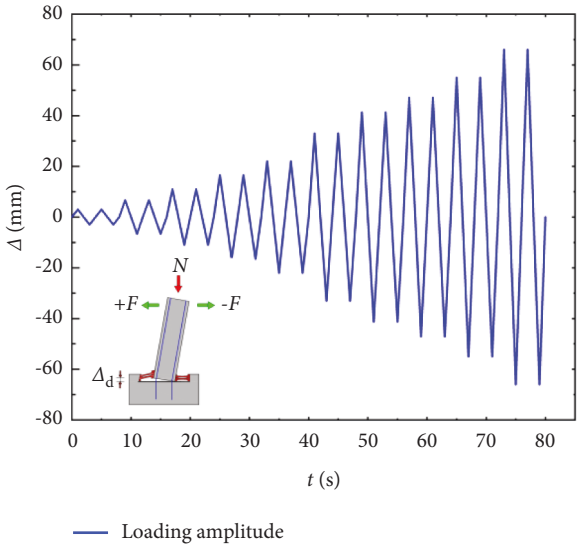

Figure 8: Loading scheme.

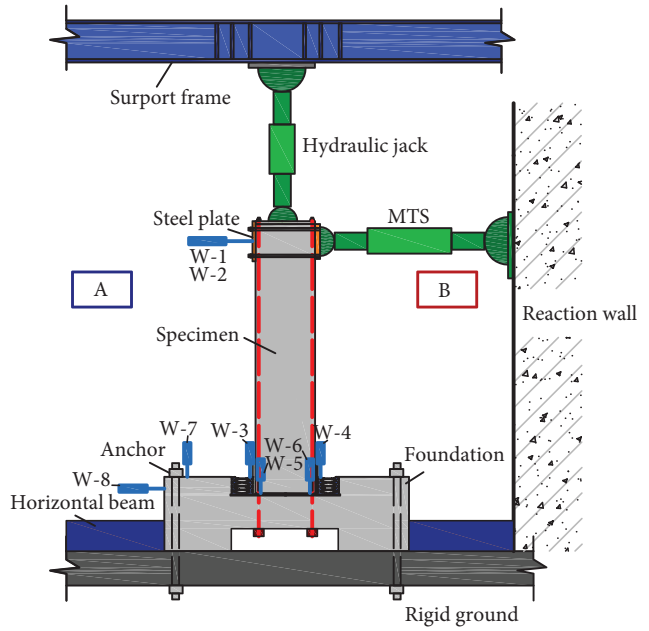

Figure 9: The schematic of pseudo-static loading test and measurement plan for displacement gauges.

reached 48 mm, the REDs were obviously deformed, and at the same time, the column bottom was lifted to 8 mm, and horizontal microcracks appeared in the concrete column above the protective steel plate on side A. When the peak displacement reached 63 mm (about the drift of 1/25), the RED produced a large sound from the friction phenomenon, accompanied with a large deformation, as shown in Figure 11(d). The cracks in the concrete column did not continue developing, and the prestress loss of prestressed tendons was about 41.4 %.

When reaching the rotation angle of 1/25, the concrete in HRC was not crushed due to the protection of pre-embedded steel plates, the REDs were greatly deformed, the thread of the embedded bolt did not be forced to change, and the prestress loss of prestressed tendons was small. After surpassing the rotation angle of 1/25, the loading was continued applying with 2 cycles per stage and a displacement increment of 5 mm, to prove the excellent ERPs of the RED-HRCs. When the peak displacement reached 88 mm, the concrete on side B was seriously deformed, beginning to fall off and gradually quit working. The HRC itself was not damaged, and the prestress loss of prestressed tendons was about 75 %, but the prestressed tendons remained elastic. When the peak displacement reached 107 mm (1/15), the REDs completely quit working, and then the test stopped.

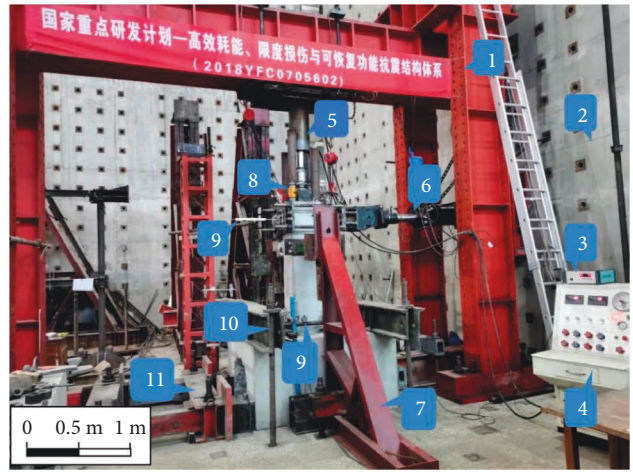

Figure 10: Experimental layout. 1, loading frame. 2, reaction wall. 3, statical strain indicator. 4, control table. 5, hydraulic Jack. 6, 500 kN actuator. 7, lateral support. 8, load sensor. 9, displacement gauge. 10, fixed beam. 11, horizontal support beam.

Table 5: The test case design and loading scheme.

Case number (type)	The initial tension of prestressed tendons (kN)	Prestressed tendon diameter (mm)	Axial compression ratio	RED thickness (mm)	Loading scheme
Specimen 1 (RED-HRC) (Z1-0.1-0.4-10)	90	15.2	0.1	10	Force-control for 1 cycle of the first loading step. Displacement-control for 2 cycles for other loading steps.
Specimen 2 (RED-HRC) (Z2-0.1-0.5-10)	110	15.2	0.1	10	
Specimen 3 (RED-HRC) (Z3-0.1-0.4(12.7)-10)	90	12.7	0.1	10	
Specimen 4 (RED-HRC) (Z4-0.3-0.4-10)	90	15.2	0.3	10	
Specimen 5 (RED-HRC) (Z5-0.1-0.4-6)	90	15.2	0.1	6	
Specimen 6 (RED-HRC) (Z6-0.1-0.4-14)	90	15.2	0.1	14	
Specimen 7 (RED-ORC) (Z7-0.1-/-10)	—	—	0.1	10	

From the experimental phenomena, the goal of "no damage to the main structure, controllable entire damages, energy dissipation concentration in the replaceable components, and fast recovery of structure-function after earthquakes" can be achieved.

5.2. Experimental Result Analysis

5.2.1. Hysteresis Curves. The force-displacement hysteresis curves at the top of each specimen for the 7 test cases, shown in Figure 13, have the following characteristics:

(1) Under the combined action of prestressed tensions and REDs, all RED-HRCs exhibit the "double-flag shape" hysteresis curves, indicating excellent ERPs and seismic properties. For a typical hysteresis curve, in the initial stage, the contact surface between the HRC and the foundation is always in the closed state, and the entire RED-HRC is in the elastic state. With the increase of the vertex peak displacement for each loading cycle, the HRC bottom begins to rise and fall alternatively, and the contact surface between the HRC and the foundation alternatively opens and closes; meanwhile, the force-displacement hysteresis curve for each specimen begins to appear like "double-flag shape." As the vertex displacement continues increasing, the hysteresis loop keeps developing, indicating that the capacity of RED-HRC holds enhancing, while the stiffness begins to degrade. The elastic restoring forces are always provided based on the inherent material properties of prestressed

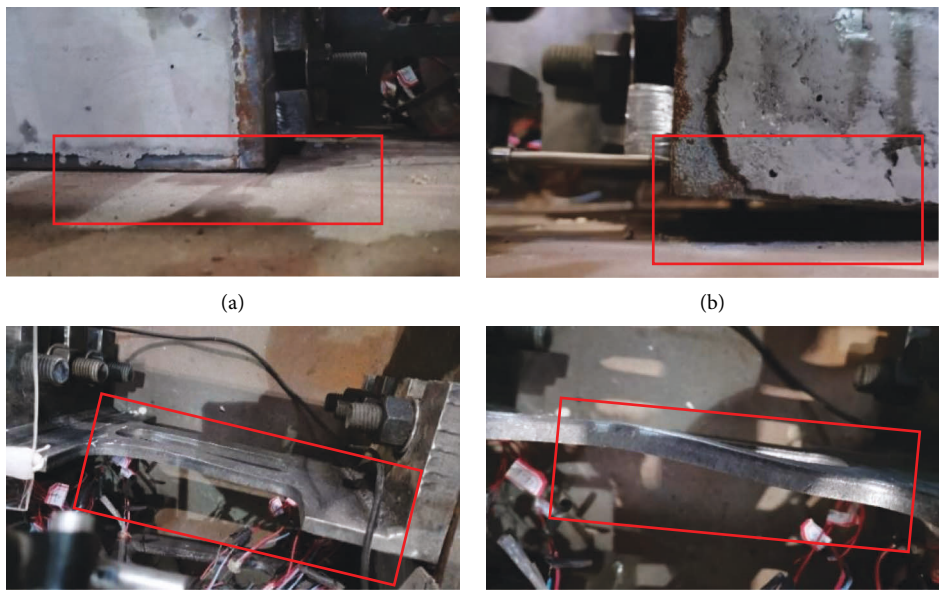

(a) (b) (c) (d)

Figure 11: The deformation of RED during testing. (a) Rocking stage. (b) Uplift of the HRC bottom. (c) The initial deformation of RED. (d) The obvious deformation of RED.

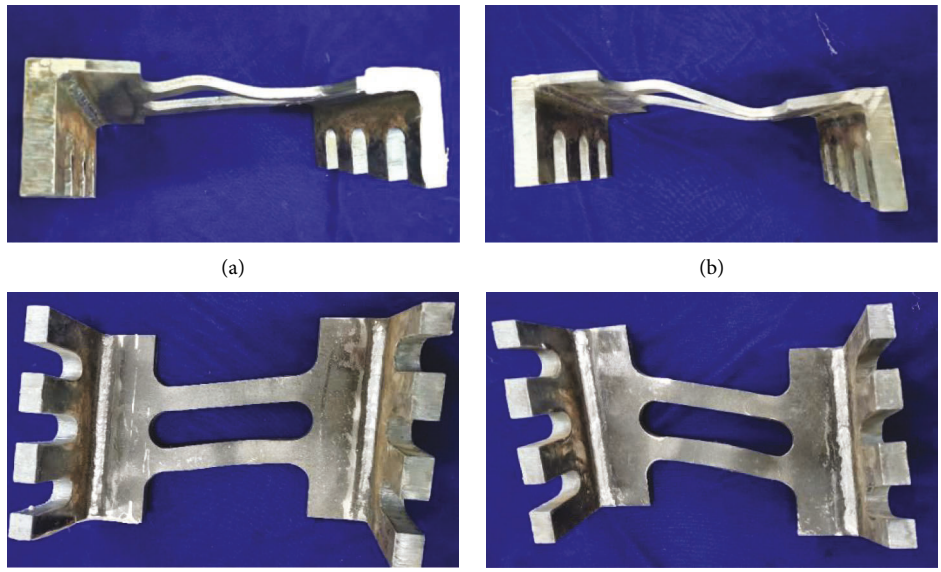

(a) (b) (c) (d)

Figure 12: The failure of RED after testing. (a) Lateral view 1. (b) Lateral view 2. (c) Front view 1. (d) Front view 2.

tendons. Therefore, the specimens have almost no residual deformation left if the restoring forces are high enough, which verifies the excellent ERPs and seismic properties for the proposed RED-HRCs.

(2) With the increase of loading steps, the area of the hysteresis loop for the last cycle is always smaller than that for the next one during the two cycles for the same loading step. This is because the cyclic loading may lead to the accumulation of damage to the components and the slippage at two anchorage ends of prestressed tendons, resulting in the degradation of both strength and stiffness of the specimens. Under the continuous cyclic loading, the damage accumulation of REDs is gradually serious, therefore, the peak horizontal bearing capacity and the slope of the curve for the next cycle are always lower than that for the last cycle with the increase of the loading steps.

(3) Under the premise of other same conditions, the increase of both the cross-sectional area and initial

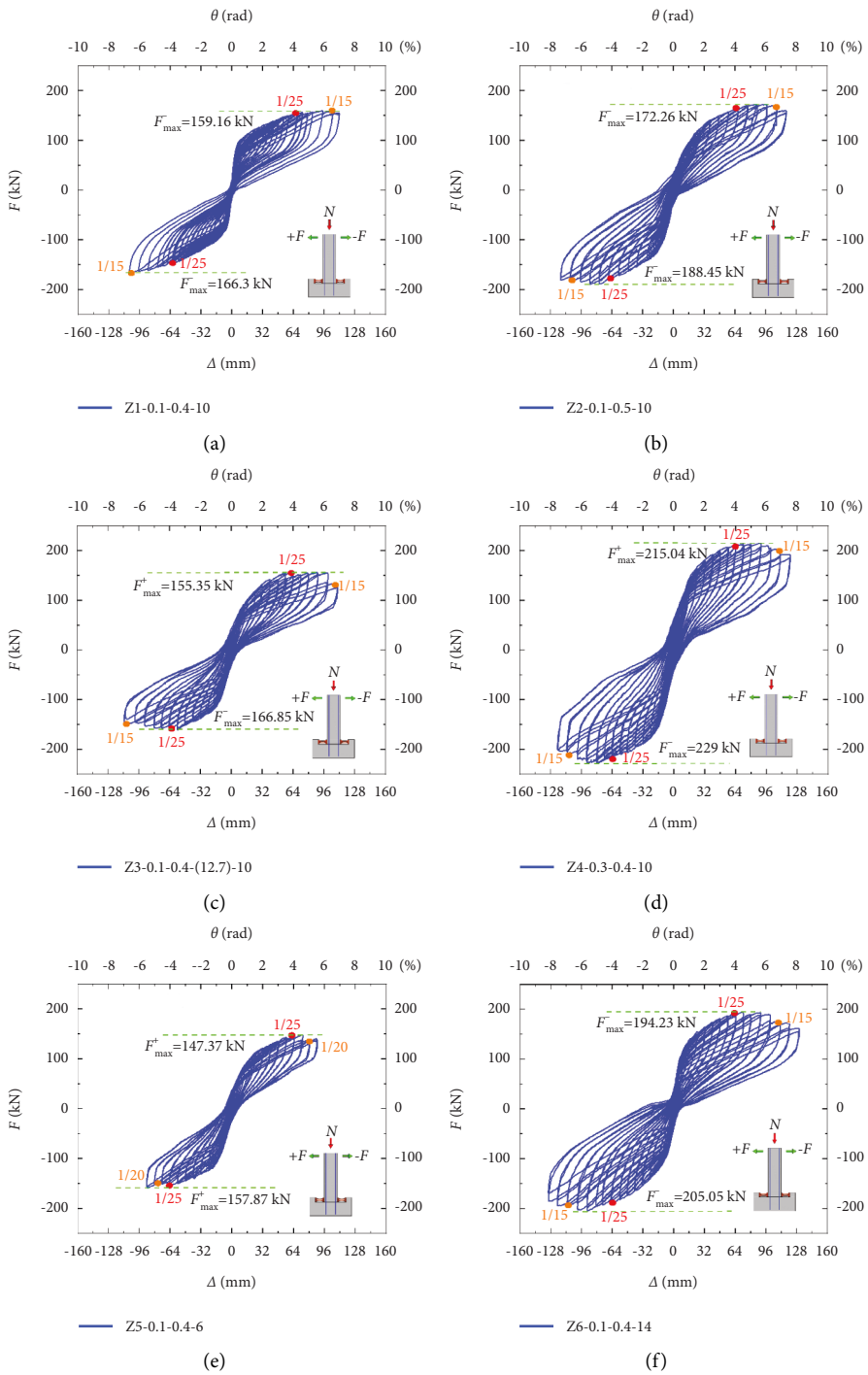

Figure 13: Continued.

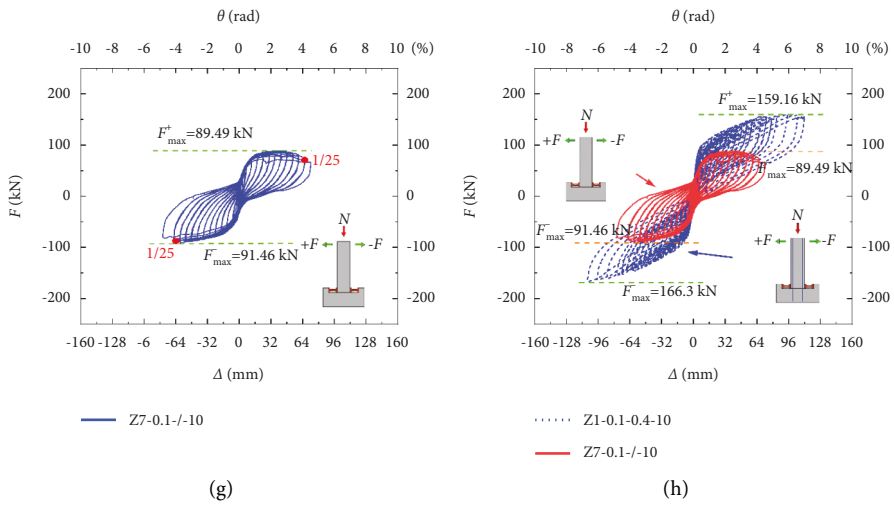

(g) (h)

Figure 13: Hysteretic curves of different working cases. (a) Specimen 1. (b) Specimen 2. (c) Specimen 3. (d) Specimen 4. (e) Specimen 5. (f) Specimen 6. (g) Specimen 7. (h) Comparison of force-displacement hysteresis curves of Specimen 1 and Specimen 7.

prestress value of prestressed tendons can improve horizontal bearing capacities of RED-HRCs and weaken stiffness degradations, shown in Figures 13(a)–13(c). The elastic restoring forces provided by prestressed tendons with greater cross-sectional areas may increase with the development of rotation angle θ, meanwhile, the concrete cracking is sufficiently suppressed. Energy dissipations are mainly concentrated in the REDs, therefore, the energy dissipation capacities for Specimen 1 and Specimen 3, shown in Figures 13(a) and 13(c), are basically the same due to the same parameters of the REDs. Moreover, increasing the initial value of prestressing force can also improve the early stiffness of the structure and self-centering ability, as shown in Figures 13(a) and 13(b). With the increase of rotation angle θ, the horizontal bearing capacities for Specimen 1 and Specimen 2 gradually tend to be consistent, and stiffness degradations are almost the same. As the hysteresis curve is in elastic stage, the HRC with a smaller initial prestressing force has better energy dissipation. The larger initial prestressing force will limit the cracking of the concrete, resulting in weakening the energy dissipation. As the hysteresis curve reaches the plastic stage, the energy dissipation of the RED-HRCs for Specimen 1 and Specimen 2 tends to be the same. Meanwhile, the cumulative energy dissipation is basically the same because of the same parameters of the REDs.

(4) From the comparison of Figures 13(a) and 13(d), the mechanical properties of the RED-HRCs are different in altering axial compression ratios. With the increase of axial compression ratios, the areas of the hysteresis loops are not obviously changed, and the hysteresis curves of the RED-HRCs are becoming plumper with sufficient energy dissipation. In addition, the horizontal bearing capacity also increases, that is, the axial compression ratio is proportional to the entire stiffness of RED-HRCs, and the stiffness degradation ability decreases. The cumulative energy dissipation is quite different mainly due to the compression failure and cracking of concrete. Meanwhile, the energy dissipation is still mainly concentrated in the REDs, which is positively correlated with axial compression ratios.

(5) From the comparison of Figures 13(a), 13(e), and 13(f), the RED-HRCs with both elastic and plastic stages in the two-way loading process are greatly influenced by the thickness of REDs. The trends of hysteresis curves are consistent, and the hysteresis loops are relatively plumper and have better energy dissipation. With the increase of thickness of REDs, horizontal bearing capacities are improved, and REDs' working states are changed from two ribs working together to two ribs working in sequence with the increase of rotation angle θ. The thickness of REDs which has little effect on the self-centering ability can obviously reduce the stiffness degradation rate and be proportional to the energy dissipation.

(6) From Figures 13(a), 13(g), and 13(h), the RED-HRCs have better self-centering capabilities than those of ordinary rocking columns (ORCs) because the application of prestressed tendons can reduce stiffness degradation abilities, improve horizontal bearing capacities, and increase limit angles of rotation for RED-HRCs. The hysteresis curves of two types of RED-HRCs are very plumper, and energy dissipations are mainly concentrated in REDs. Due to the concrete cracking of the ORC, the energy dissipation is relatively different from others. Meanwhile, elastic restoring forces provided by prestressed tendons can reduce the occurrence of cracks, which can avoid structural damage and achieve the goal of "the damage of component being concentrated and controllable," showing excellent ERPs and seismic properties for RED-HRCs.

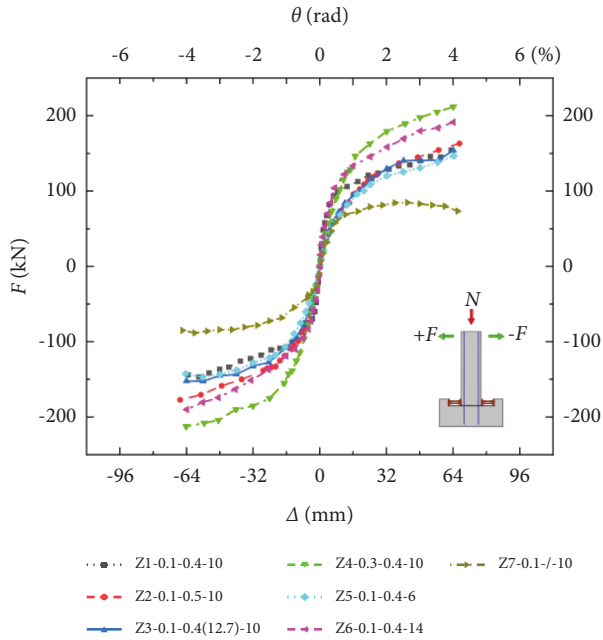

Figure 14: Comparison of skeleton curves (1/25).

5.2.2. Skeleton Curves. For the top of the RED-HRC, the force-displacement skeleton curves of the hysteresis curves for Specimen 1 to Specimen 7 are shown in Figure 14.

From Figure 15, the stiffness degradations of the specimens in the 7 working cases have similar developing trends, which are, in initial stages, when the rotation angles are small, the stiffness degradations of the specimens that have rapidly decreasing slopes, and with the increase of the rotation angles, the stiffness degradations of the specimens gradually tend to be gentle. When the rotation angles reach 1/25, the stiffness decreases to 10 % ~ 20 % of the initial stiffness. In addition, axial compression ratios and initial values of prestressing forces can effectively slow down the rates of stiffness degradations, for example, the stiffness degradation of Specimen 7 is altered with the steepest slope because of the lack of prestressed tendons, which means, on the other hand, prestressed tendons can be beneficial for slowing down the stiffness degradation.

5.2.3. Stiffness Degradation Curves. The stiffness degradation curves for Specimens 1 to 7 are shown in Figure 15.

From Figure 15, the stiffness degradations of the specimens in the 7 working cases have similar developing trends, which are, in initial stages, when the rotation angles are small, the stiffness degradations of the specimens that have rapidly decreasing slopes, and with the increase of the rotation angles, the stiffness degradations of the specimens gradually tend to be gentle. When the rotation angles reach 1/25, the stiffness decreases to 10% ~ 20% of the initial stiffness. In addition, axial compression ratios and initial values of prestressing forces can effectively slow down the rates of stiffness degradations, for example, the stiffness degradation of Specimen 7 is altered with the steepest slope because of the lack of prestressed tendons, which means, on the other hand, prestressed tendons can be beneficial for slowing down the stiffness degradation.

5.2.4. Hysteresis Prestressing Forces. For the RED-HRCs, the prestressing force hysteresis characteristics of prestressed tendons are influenced by the peak rotation angles. Since peak rotation angles under minor earthquakes are usually small, the loss of prestress in prestressed tendons is relatively small in this case, and the prestressing force will be linearly changed. However, as peak rotation angles under major earthquakes are great, the loss of prestress in prestressed tendons will be significant, resulting in a nonlinear change of the prestressing forces during the rocking process. The effect of the loss of prestressing of prestressed tendons is validated by the experiment. Due to the limitation of the paper, Specimen 5 is taken as an example to show the loss of prestressing during rocking process. The relationship between the prestressing force and the peak displacement of Specimen 5, which is measured by the load sensor in one prestressed tendon, is shown in Figure 16.

The prestressing forces generated by prestressed tendons on both specimen sides during the cyclic loading are basically symmetrical due to the symmetrical locations of the prestressed tendons. In the initial stage of the test, the change of the prestressing force value is only caused by the elastic deformation of the prestressed tendons. Meanwhile, the contact surface between the RED-HRC and the foundation is in a completely closed state under the combination of axial forces including the initial prestressing forces and the gravity of HRC, and the initial value of prestressing force remains unchanged. When the HRC reaches the critical compression state with the small uplift at the HRC bottom, the contact surface opens on one side and closes on the other side, and the pressed tendons are in the elastic stage. Since the stiffness of the HRC is much greater than that of the prestressed tendons and the REDs, it is assumed that both

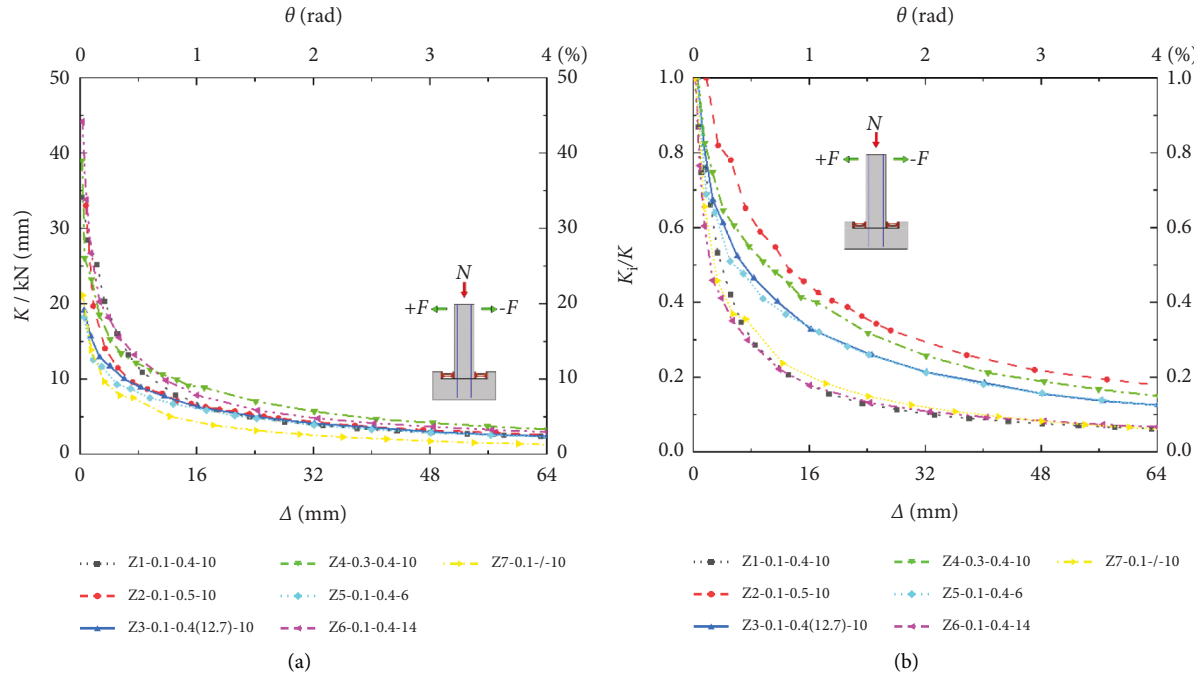

Figure 15: Stiffness degradation curves (1/25). (a) K-Δ; (b) K_i/K-Δ.

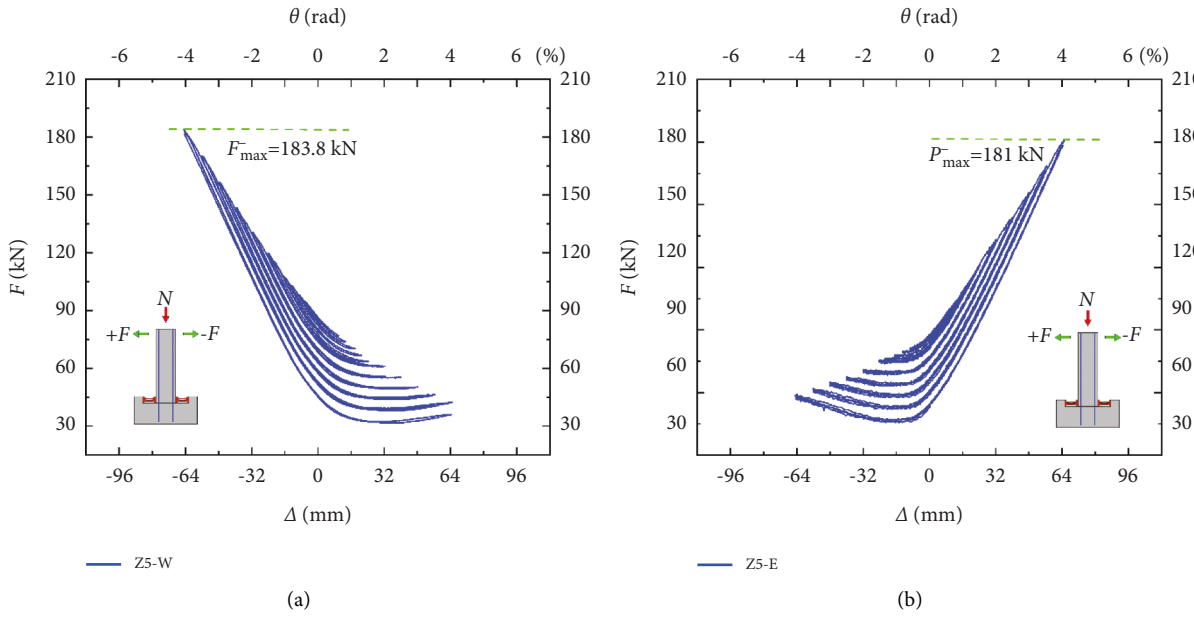

Figure 16: The prestressing forces vs. displacements for Specimen 5. (a) For the tendon at side A. (b) For the tendon at side B.

the uplift of the HRC and the deformation of prestressed tendons are proportional to the lateral displacement at the top of the HRC. As increasing the lateral peak deformation for each loading cycle, the loss of the prestress of prestressed tendons is gradually increasing due to the slippage and looseness at the two anchorage ends of the prestressed tendons. Therefore, the initial prestressing forces have been decreased after the test. The initial prestressing loss for each test case is shown in Table 6. The prestressed tendons for these test cases can work perfectly as the peak rotation angles are small, but the prestressed tendons can also work with the loss of initial prestress as the peak rotation angles are large. The mean value of the loss of prestressing is about 36.3% for the peak rotation angle of 1/25 which represents the limitation of drift for the structural member under extremely major earthquakes.

5.2.5. Energy Dissipation Curves. The equivalent viscous damping coefficient h_c curves and cumulative energy dissipation coefficient ζ curves of Specimens 1 to 7 are shown in Figures 17–20.

Table 6: The test results of prestressing forces in each working case.

Case number	Prestressed initial resultant force (kN)	Prestressed strand diameter (mm)	Residual prestress (kN)	Maximum prestress (kN)	Percentage loss of prestress (%)
Specimen 1	357.8	4×15.2	209.8	496.8	41.4
Specimen 2	410.3	4×15.2	289.2	574	29.5
Specimen 3	365.8	4×12.7	264.1	467.8	27.8
Specimen 4	369.4	4×15.2	213.3	497.9	42.5
Specimen 5	367.2	4×15.2	237.2	490.3	35.4
Specimen 6	366.3	4×15.2	215.9	515.2	41.1

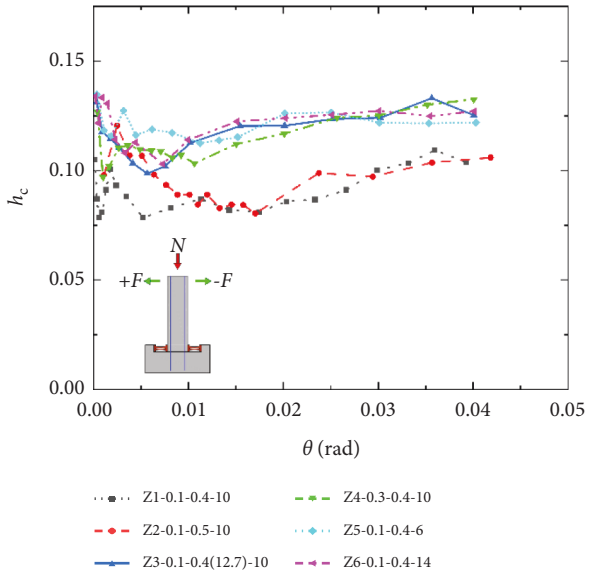

Figure 17: Comparison of equivalent viscous damping coefficient h_c curves.

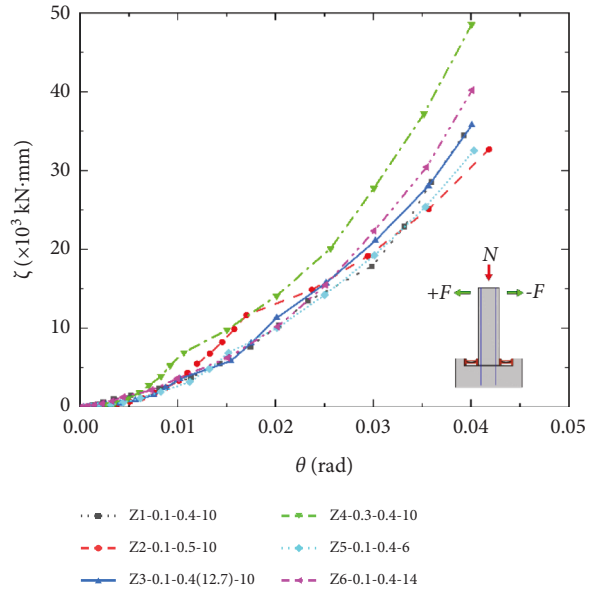

Figure 18: Comparison of cumulative energy dissipation coefficient ζ curves.

In the RED-HRC tests, the force-displacement hysteresis curves, in general, are relatively plumper, indicating that the REDs have good energy dissipation capacities. With the increase of the lateral loading, hysteresis loop areas of the RED-HRCs increase, denoting that the energy dissipation capacities have further improved due to much more plastic deformations. The h_c–θ curves of the RED-HRC have basically the same trend, showing a relatively stable trend. With the increase of θ, the plastic deformations of the RED-HRCs are becoming larger with more energy dissipating capacities. Meanwhile, the cumulative energy dissipation curves of the RED-HRCs basically keep almost the same state when θ is less than 0.005.

The thickness of the REDs has an obvious influence on the energy dissipation, as shown in Figure 17. The REDs with the same thickness almost have the same energy dissipation, and the REDs with the larger thickness have a higher energy dissipation capacity because the energy dissipation for RED-HRCs concentrates upon the REDs. In addition, the trend of the hysteresis curves is consistent when the thickness of the energy dissipator is changed. The equivalent viscous damping coefficient h_c and cumulative energy dissipation coefficient ζ are proportional to the thickness of the energy dissipator. The thickness of REDs has little effect on the self-centering capacity and the rate of stiffness degradation. Meanwhile, the horizontal ultimate capacity of the RED-HRCs is also significantly improved with the increase of θ and thickness of the RED.

The axial compression ratios also have a certain influence on the energy dissipation, while the cross-sectional area of prestressed tendons, the initial prestressing force, and other factors have little effect on the energy dissipation of the RED-HRCs.

The comparison of Specimen 1 and Specimen 7 shows that the arrangement of prestressed tendons has a certain influence on the energy dissipation capacity although the energy dissipation is mainly concentrated in the REDs, as shown in Figure 19. An upward trend of the h_c–θ curve for Specimen 7 and a stable trend for Specimen 1 are shown. The energy dissipation of Specimen 7 is generated by both the REDs and concrete cracking of the rocking column, and the elastic restoring force provided by the prestressed tendons in Specimen 1 can effectively reduce the occurrence of cracks in the main structure, reducing the energy dissipation. Therefore, the energy dissipation is mainly concentrated in the REDs for the RED-HRCs because the prestressed

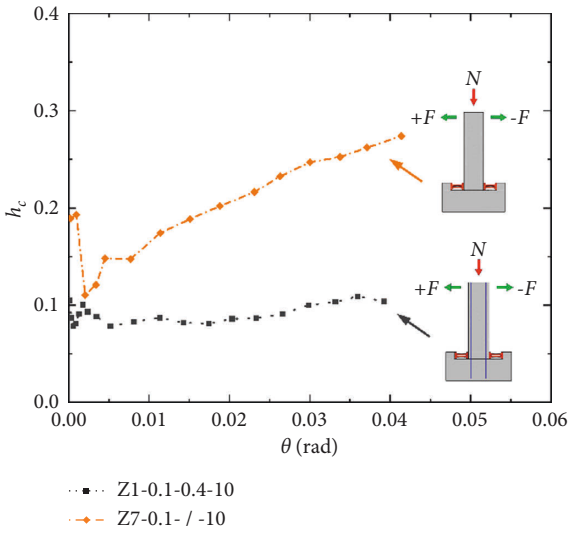

Figure 19: Comparison of equivalent viscous damping coefficient h_c curves of RED-HRC and RED-ORC.

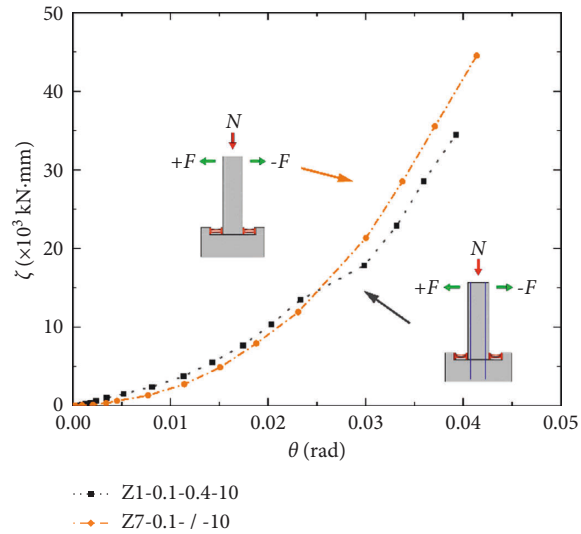

Figure 20: Comparison of cumulative energy dissipation coefficient ζ curves of RED-HRC and RED-ORC.

tendons can significantly reduce concrete cracking in the HRCs and the corresponding energy dissipation. However, the cumulative energy dissipation in the early stage of the two working cases is basically the same because of no concrete cracking in the elastic deformation. The accumulative energy dissipation of Specimen 7 in the middle and late stages is higher than that for Specimen 1, which is due to the increase of the entire energy dissipation capacity caused by the cracking of concrete in the main structure of Specimen 7, as shown in Figure 20.

5.2.6. Deformation and Self-Centering Capability Analysis. The self-centering capability factor γ is defined to reflect the deformation and self-centering capacity.

$$\gamma = 1 - \frac{\Delta_c}{\Delta_{max}}, \tag{13}$$

where γ is the self-centering coefficient of the RED-HRC; and Δ_c and Δ_{max} are the lateral residual deformation and maximum deformation of the i-th cycle, respectively. The specific maximum deformation Δ_{max}, the residual deformation Δ_c, and self-centering capability coefficient γ of various working cases are shown in Table 7.

From Table 7, the RED-HRCs have good resilient and seismic performances. Meanwhile, the prestressed tendons were far from the ultimate strength during the test, indicating that the prestressed tendons can always maintain an elastic working state during earthquakes. The self-centering ability coefficients γ of the RED-HRCs are all about 90 %, while the self-centering ability coefficient γ of the RED-ORC is only 41.75 %, indicating that the RED-HRCs have better resilient performance than that of RED-ORC due to the prestressing effect of the prestressed tendons.

Taking Specimen 6 as an example, Figure 21 shows the relationship between the absolute residual drift θ_r or displacement Δ_r (or the relative residual drift θ_r/θ or displacement Δ_r/Δ) and the change of the rotation angle θ. Here, θ_r/θ is the ratio of the absolute residual rotation angle to the peak rotation angle of the RED-HRC. When the peak rotation is 1/25 (4 %), the residual rotation θ_r is about 0.46 %. The relative rotation is always kept below 20 % during the entire loading. Figure 22 reflects the relationship between the uplift δ at the RED-HRC bottom and the lateral force F, and the residual uplift is defined as δ_r. The direction for the uplift is defined as the sign of "+" which means that the side of the rocking column is in tension and the column bottom uplifts; the direction for the moving down is defined as the sign of "–" which means that the side of the rocking column is in compression. When the rotation angle θ returns to 0 (the original position), the rocking column bottom uplift Δ_r and the horizontal bearing capacity F are both near 0, indicating that the RED-HRC has a good self-centering performance which can avoid being damaged.

6. Finite Element Analysis

6.1. Finite Element Model Verification. A numerical simulation analysis was carried out based on ABAQUS software, aiming at further investigating the energy dissipation of the REDs. Therefore, a finite element analysis (FEA) is performed according to the parameters of the proposed RED-HRCs.

In the finite element model (FEM), the damage constitutive relationship for concrete and the bilinear kinematic hardening constitutive relationship for rebar are used which are suggested by the code in China. The solid part of the model adopts the C3D8R element, and the stressed reinforcement and the prestressed reinforcement adopt the truss element. The contact relationship between the conventional rebar and concrete is set as embedded region, and the contact relationship between the prestressed tendon and concrete is handled as follows: a small pad is used to simulate the anchor at the top of the column and the bottom end of

Table 7: The maximum deformation, residual deformation, and self-centering capacity coefficients in each test working case.

Case number	Maximum deformation, Δ_{max} (mm)	Residual deformation, Δ_c (mm)	Self-centering capability factor, γ (%)
Specimen 1	63.21	3.21	94.92
Specimen 2	67.09	7.06	89.47
Specimen 3	64.12	6.77	89.44
Specimen 4	64.75	6.02	90.70
Specimen 5	64.18	9.11	85.81
Specimen 6	64.15	4.49	93.00
Specimen 7	66.20	38.56	41.75

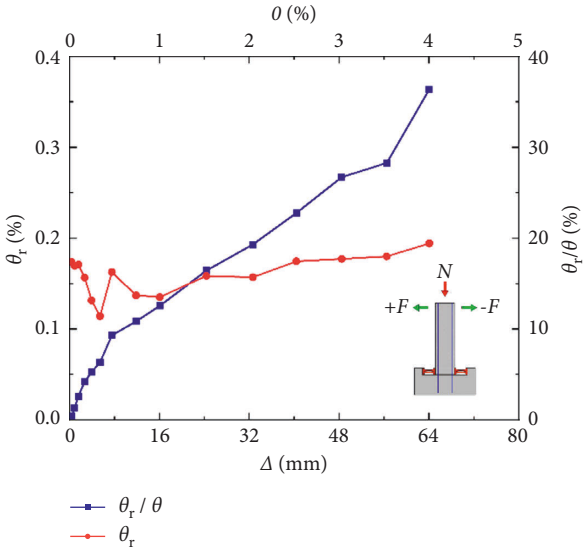

Figure 21: The relationship between θ and θ_r.

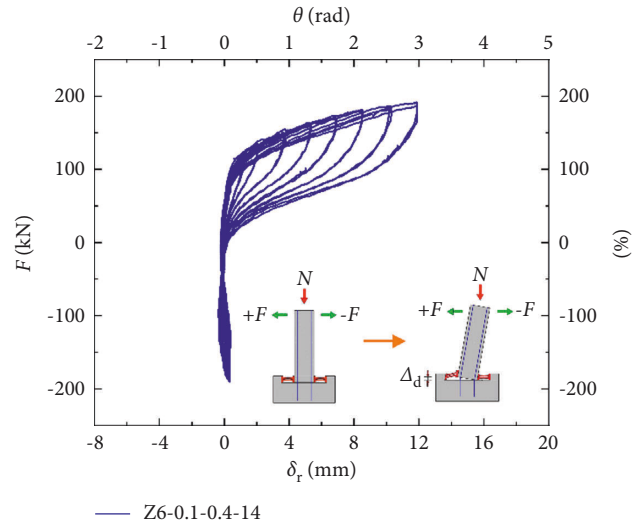

Figure 22: The relationship between F and δ.

the foundation corresponding to the prestressed tendons. The cushion layer and the anchor are used to fix the prestressed tendons. The anchorage and prestressed tendons are both set as elastic materials. The "cooling method" is used to apply prestress in the prestressed tendons according to the principle of thermal expansion and contraction. Concrete is set as the concrete damaged plasticity. The contact surfaces of other components are set as hard contact in the normal direction and the friction coefficient in the tangential direction. The specific friction coefficient is set according to the material properties of the contact surface. The settings such as loading methods and boundary conditions are as the same as those of the after-mentioned experiments.

To verify the accuracy of the established finite element model (FEM), the typical test result of the RED-HRC for Case 6 (Specimen 6) was selected for comparison with the numerical simulation. The comparison for hysteresis curves of FEA simulation and experiment is shown in Figure 23.

From Figure 23, the general trends for both the hysteresis curves match very well. There is a "pinching phenomenon," which comes from the relative slip between the contact surface and the lateral deformation of prestressed tendons during the loading. Moreover, the initial stiffness of the RED-HRC in the FEA result is a little higher than the experimental one due to the ideal contact surfaces in the FEA on one hand, and the experimental contact surface with initial tiny defects, on the other hand, causing the slip during the experimental loading process. In addition, the curve of the experimental result is relatively plumper, while the simulation curve has a better pinch effect. This is because the boundary conditions and the bolt pre-tightening force are ideal in the FEA, generating a certain error in the experimental installation and loading. Since the numerical simulation and experimental results are in good agreement, and the general trends are basically the same, which can correctly reflect the mechanical properties of the proposed RED-HRCs such as the horizontal bearing capacity and energy dissipation capacity corresponding to the experimental conditions.

6.2. Energy Dissipation Capacity of RED. Based on the above analysis, the energy dissipation capacity of RED is dominated for the RED-HRCs under pseudo-static loading. Therefore, the effects of bolt preload and thickness of RED on the mechanical properties of RED-HRCs under a monotonic loading should be importantly investigated. For this purpose, a total of 4 cases are selected to study the effect of different bolt pre-tightening forces on the energy dissipation of REDs, shown in Table 8. In the established FEA models, the bolt diameter of 24 mm is unchanged, and three kinds of preloads of 0, 100, and 300 kN are considered, respectively. Two contact surfaces of hard contact with friction and fixed connection contacts are selected.

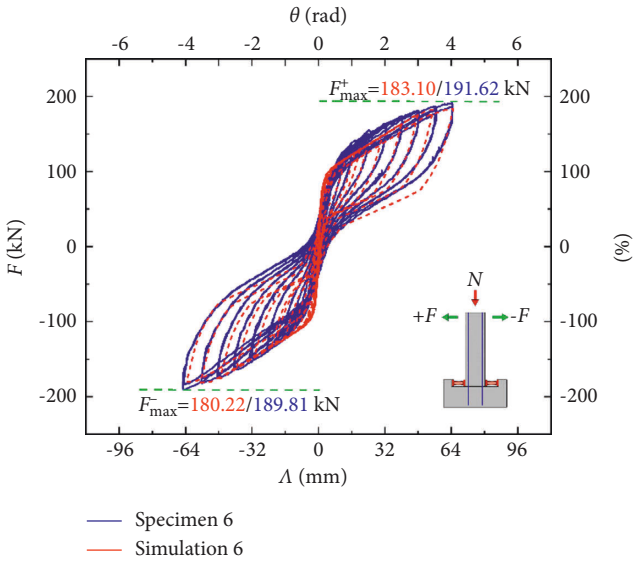

Figure 23: The comparison for hysteresis curves of FEA simulation and experiment.

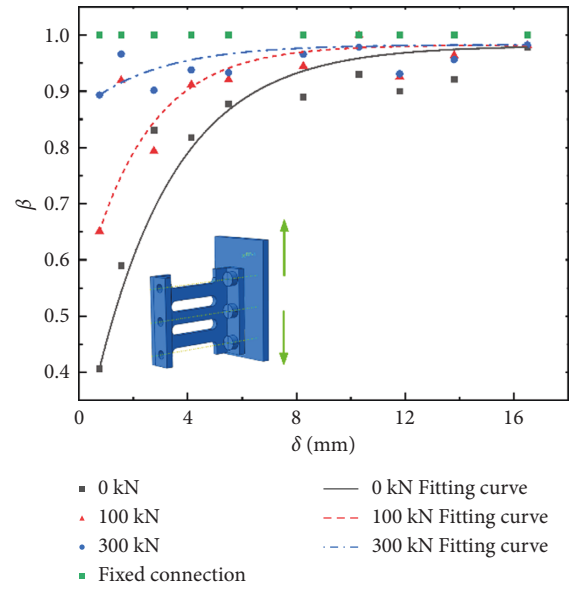

Figure 24: The relationship between yield energy dissipation coefficient β and displacement δ.

Table 8: The design of bolted connection RED working cases.

Cases	Bolt diameter	Contact settings	Preload (kN)
1	24	Hard contact and friction	0
2	24	Hard contact and friction	100
3	24	Hard contact and friction	300
4	—	Fixed connection	—

The yield dissipation factor β is selected and used to reflect the effect of different bolt preloads on the yield dissipation energy of REDs.

$$\beta = \frac{A_L}{A_T}, \tag{14}$$

where β is the yield dissipation coefficient, A_L is the yield dissipation energy generated by the RED when considering the bolt preload and friction as well as slip, and A_T considers the yield dissipation energy generated by RED without the interfacial friction and slip.

The relationship between yield dissipation factor β and displacement δ is shown in Figure 24. The influence of different bolt preloads on the yield energy dissipation of RED is mainly focused on the initial stage of loading for the small displacement δ. For the case of bolt preload of 0 and small displacement, the ratio of yield energy dissipation to friction energy dissipation is about 2 : 3, and the friction energy dissipation is dominant. For the case of bolt preload of 100 kN, the ratio of yield energy dissipation to friction energy dissipation is about 6.5 : 3.5, and the yield energy dissipation is dominated in turn. The ratio of yield energy dissipation to friction energy dissipation is about 9 : 1 for the case of bolt preload of 300 kN. For all cases, with the increase of displacement δ, the yield energy dissipation gradually increases, and the yield energy dissipation coefficient β gradually tends to the value of 1, the same as the case of fixed interfacial connection.

6.3. Influence of Thickness of REDs. Through the above experimental analysis, the shape and strength of RED have a significant effect on the energy dissipation capacity and self-centering capacity, as well as lateral stiffness resistance of the proposed RED-HRCs. For the same shape and strength of RED, the selection of the thickness of RED will be helpful for determining yield energy dissipation coefficient β which is quite important to the design of RED. Therefore, two kinds of thickness of RED are considered to take the numerical simulation to investigate the failure mode and basic mechanical properties under pseudo-static loading. The deformation for the RED thickness of 10 mm in FEA simulation and experiment are shown in Figures 25 and 26, respectively.

The skeleton curves and cumulative energy dissipators coefficient ξ curves based on the hysteresis curves for RED-HRCs with the RED thickness of 6 mm and 10 mm are shown in Figures 27 and 28, respectively, showing that the early stiffness and strength, as well as of the energy dissipation capacity of RED-HRCs, are significantly improved with the increase of RED's thickness under the premise of other conditions being the same. However, the self-centering ability was reduced. This is because the equivalent restoring forces provided by the prestressed tendons should overcome the different RED's resistances due to different thicknesses of REDs, resulting in higher initial stiffness, larger bearing capacity, and energy dissipation capacity, but more obvious residual deformation with the increase of the thickness of REDs.

7. Design Method and Process

The design of RED-HRCs should obey three seismic fortification levels and two-stage design methods which are suggested by "Code of Seismic Design of Buildings of

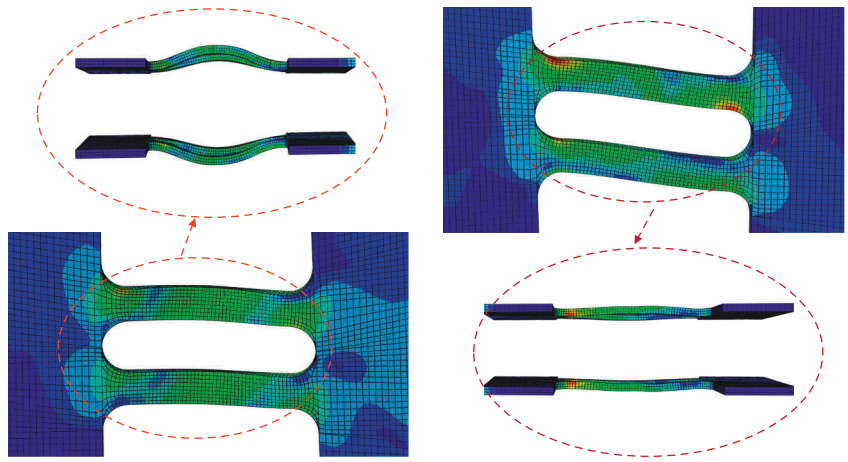

Figure 25: Deformation of RED for FEA simulation.

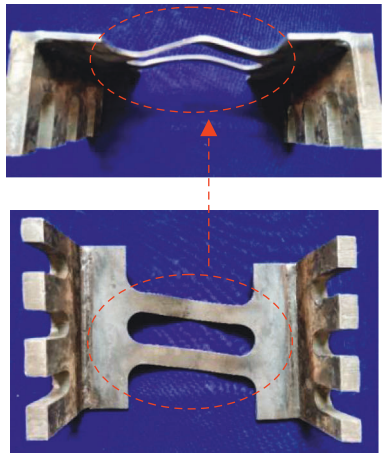

Figure 26: Deformation of RED on the uplift side after the experiment.

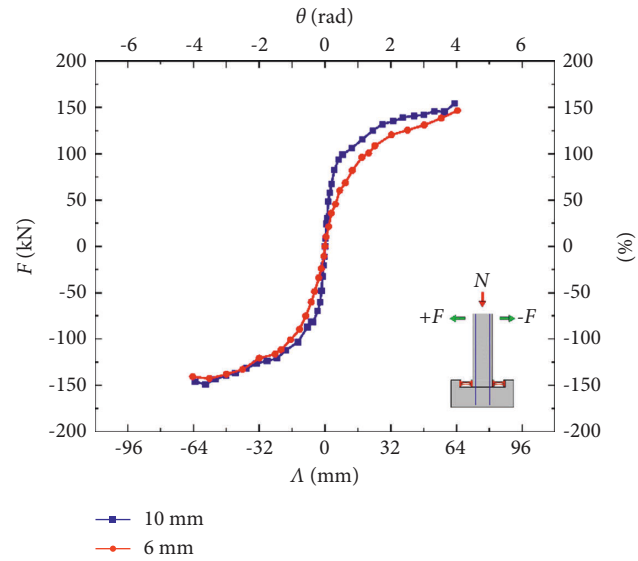

Figure 27: Comparison of skeleton curves of specimens with different energy dissipators thickness.

China." Therefore, the design should contain two stages: (1) the elastic design stage under minor earthquakes (the first seismic fortification level) for the first stage and (2) the elastoplastic design stage under major earthquakes (the third fortification level) for the second stage. Conventional RC structures are designed, in general, to dissipate the seismic energy through the measures and plastic deformation of the structure itself. The designed structure can meet the requirements of structural functions in the elastic range under minor earthquakes. Meanwhile, under major earthquakes, the structure that underwent plastic deformation still can meet the requirements of drift limits required by the current codes. However, through the investigation of RED-HRCs, we found that the energy dissipation of REDs and the elastic restoring force of the prestressed tendons can ensure that the main structure does not yield or damage under the earthquake actions. Because the mechanical characteristics of RED-HRCs are different from those of the traditional RC structures, which are designed to dissipate the seismic energy and limit the maximum deformation of the structure by plastic deformation of the main members, it is not applicable for the design of RED-HRCs in the elastoplastic design stage.

Therefore, for the elastic design stage, the design method of traditional RC structures can be used in the RED-HRCs to determine concrete strength, cross-sectional dimensions, and the arrangement of load-bearing members according to the performance index of the structure. However, the design method should be adjusted for the second design stage according to the properties of the proposed RED-HRCs.

The most obvious property of the RED-HRCs is the predominant rotation due to the rocking process in earthquakes. Excessive deformation might lead to the failures of nonstructural components, even collapse or overturning of the structure under major earthquakes, which will affect the resilient performance of the structure. Therefore, the design objective for the elastoplastic stage is to limit the maximum rotation angle and residual deformation of the RED-HRCs in major earthquakes. Therefore, the placement of limit control devices at the base of RED-HRCs is one of the effective ways to limit the maximum rotation of the structure.

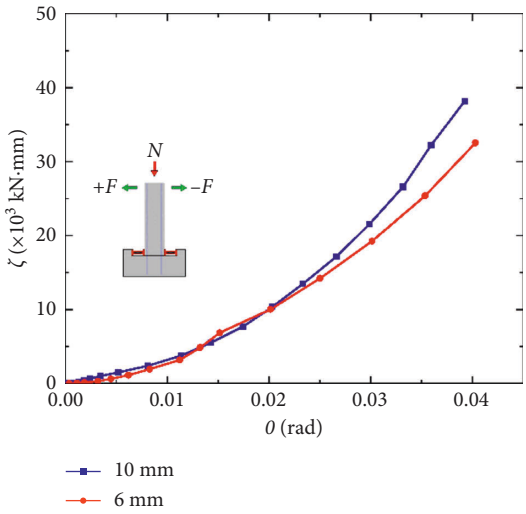

FIGURE 28: Comparison of cumulative energy dissipators coefficient ζ of specimens with different energy dissipator thickness.

The minimum prestressing force required for the RED-HRCs is also related to the strength of the RED, the minor earthquake required by the code, and the vertical load. Meanwhile, it must be ensured that the friction of the contact surface between the HRC and foundation must be greater than the interfacial shear force generated by an external load, and the yield moment at the contact interface should be larger than the combined moment generated by the minor seismic action and vertical loads, as shown in the following equation:

$$N + P_0 \geq \frac{\left(V_G^d + V_e^d\right)}{\mu_f}, \tag{15}$$

$$M_y \geq M_G^d + M_e^d, \tag{16}$$

where N and P_0 denote the vertical load and the initial prestressing force, respectively; V_G^d and V_e^d are the shear forces generated by the vertical load and minor seismic action, respectively; μ_f represents the friction coefficient between the protective steel plates; M_y is the yield moment at the bottom of the RED-HRC; and M_G^d and M_e^d are the bending moments generated by vertical load and minor seismic action, respectively.

The energy dissipation behavior of RED-HRC is mainly concentrated in the REDs which also provide a certain amount of resisting moment. Therefore, the general resisting moment at the bottom of RED-HRC includes the self-centering moment generated by the combined effect of prestressing and axial forces and the hysteresis moment produced by the RED. The New Zealand code requires that the hysteresis moment and the self-centering moment must meet certain proportional requirements in the resisting moment of the joints, as shown in the equation:

$$\frac{\left(M_{pt} + M_G\right)}{M_s} \geq 1.15, \tag{17}$$

where M_{pt} and M_G are the self-centering moments provided by prestressed tendons and vertical loads, respectively; M_s is the hysteresis moment provided by REDs. Certain structural measures are also required to ensure that the maximum deformation of the RED-HRCs is less than the design target.

In addition, the prestressed tendons should be always kept in the elastic range. Once the prestressed tendon "yields," it will reduce its own elastic restoring force for the RED-HRC, affecting the horizontal resistance of the contact surface, and the maximum deformation of the RED-HRC, which endanger the strength and stiffness of the RED-HRCs. Therefore, a detailed calculation of the maximum stress for each prestressed tendon is required in the design stage.

8. Conclusions

(1) The RED-HRC proposed in the paper is simple and well-defined. The prestressed tendons provide elastic restoring forces, and the REDs consume energy efficiently so that the goal of "no damage to the main structure, controllable entire damages, replaceable member, easy installation, and fast recovery of structure-function" can be achieved.

(2) Using the RED's yield state as the control point, the corresponding relationship $f(M, \theta)$ between the overturning moment M and the rotation angle θ of the RED-HRCs is established. The correspondence shows that the control point of overturning moment M is positively correlated with the prestressing force provided by the prestressed tendons and the strength of REDs and increases with the increase of the rotation θ.

(3) The proposed RED-HRC has an excellent capacity for energy dissipation and self-centering. The force-displacement curve displayed a typical "flag-shaped" hysteretic response. The nonlinear deformation of slip and looseness of prestressed tendons at two anchorage ends will lead to the increase of residual deformation of the RD-HRC when the rotation θ is large. The energy dissipation behavior is mainly concentrated in the REDs. The self-centering capacity of the RED-HRC is predominately determined by the prestressed tendons and REDs. Increasing the axial compression ratio will lead to concrete cracking which increases the entire energy dissipation by about 35%, therefore, the axial compression ratio also has some influence on energy dissipation. In addition, increasing the initial prestressing forces or cross-sectional area of prestressed tendons will improve the self-centering capacity and lateral stiffness of the self-centering hybrid rocking column. Different energy dissipators' thicknesses and axial compression ratios also show a positive correlation on the energy dissipation capacity of self-centering hybrid rocking columns.

(4) Different bolt preloads have an obvious effect on the self-centering and energy dissipation capacities of the RED-HRCs. When the bolt preload is small, the contact surface will preferentially produce slip and dissipate frictional energy; when the bolt preload is

large, the energy dissipation of the material itself is preferred to the slip energy dissipation of the contact surface. The slip between the contact surfaces can improve the self-centering ability of RED-HRC but reduce its lateral stiffness in the early stage.

(5) The elastic design of RED-HRC is suggested to adopt the traditional design method for RC structures in the elastic design stage. However, the elastoplastic design of RED-HRC is recommended to apply the placement of limit control devices at the HRC bottom, meanwhile, to ensure the prestressed tendons keeping in the elastic state.

Data Availability

All data included in this study are available upon request by contact with the corresponding author.

Conflicts of Interest

The authors declare that they have no conflicts of interest.

Acknowledgments

This work was partially funded by the National Key R&D Program of China with grant no. 2018YFC0705602 and no. 2017YFC1503106.

References

[1] X. L. Lv, Y. Chen, and Y. J. Mao, "New concept of structural seismic design: earthquake resilient structures," *Journal of Tongji University*, vol. 39, no. 7, pp. 941–948, 2011.

[2] Y. Zhou, H. Wu, and A. Q. Guan, "Earthquake engineering: from earthquake resistance, energy dissipation, and isolation, to resilience," *Engineering Mechanics*, vol. 36, no. 6, pp. 1–12, 2019.

[3] Y. Zhou and X. L. Lv, "State-of-the-art on rocking and self-centering structures," *Journal of Building Structures*, vol. 32, no. 9, pp. 1–10, 2011.

[4] Y. Cui, X. Lu, and C. Jiang, "Experimental investigation of triaxial self-centering reinforced concrete frame structures through shaking table tests," *Engineering Structures*, vol. 132, pp. 684–694, 2017.

[5] X. L. Lv and C. Chen, "Research progress in structural systems with replaceable members," *Earthquake Engineering and Engineering Dynamics*, vol. 34, no. 1, pp. 27–36, 2014.

[6] X. L. Lv, D. Y. Wu, and Y. Zhou, "State-of-the-art of earthquake resilient structures," *Journal of Building Structures*, vol. 40, no. 2, pp. 1–15, 2019.

[7] X. Zhao and A. Qi, "Slotted beam-column energy dissipating connections: applicability and seismic behavior," *Advances in Civil Engineering*, vol. 2021, Article ID 5530083, 2021.

[8] Y. H. Wang, Y. Feng, D. S. Huang, Z. Huang, and Z. Chen, "Restoring force model of an energy-dissipation joint in hybrid frames: simplified skeleton curve and hysteretic rules," *Advances in Civil Engineering*, vol. 2020, Article ID 7806381, 18 pages, 2020.

[9] L. H. Zhu and C. Zhao, "Self-centering steel frame systems for seismic-resistant structures," *Advances in Civil Engineering*, vol. 202020 pages, Article ID 8859881, 2020.

[10] J. I. Restrepo and A. Rahman, "Seismic performance of self-centering structural walls incorporating energy dissipators," *Journal of Structural Engineering*, vol. 133, no. 11, pp. 1560–1570, 2007.

[11] B. Erkmen and A. E. Schultz, "Self-centering behavior of unbonded, post-tensioned precast concrete shear walls," *Journal of Earthquake Engineering*, vol. 13, no. 7, pp. 1047–1064, 2009.

[12] D. Marriott, *The Development of High-Performance Post-Tensioned Rocking Systems for the Seismic Design of Structures*, University of Canterbury, Christchurch, New Zealand, 2009.

[13] A. I. Giouvanidis and Y. Dong, "Seismic loss and resilience assessment of single-column rocking bridges," *Bulletin of Earthquake Engineering*, vol. 18, no. 9, pp. 4481–4513, 2020.

[14] A. I. Giouvanidis and Y. Dong, "Quantifying seismic resilience of single-column rocking bridges - a comparative study," in *Proceedings of the 8th ECCOMAS Thematic Conference on Computational Methods in Structural Dynamics and Earthquake Engineering*, pp. 28–30, Athens, Greece, June 2021.

[15] M. T. Nikoukalam and P. Sideris, "Resilient bridge rocking columns with polyurethane damage-resistant end segments and replaceable energy-dissipating links," *Journal of Bridge Engineering*, vol. 22, no. 10, Article ID 04017064, 2017.

[16] G. W. Housner, "The behavior of inverted pendulum structures during earthquakes," *Bulletin of the Seismological Society of America*, vol. 53, no. 2, pp. 403–417, 1963.

[17] H. Roh, *Seismic Behavior of Structures Using Rocking Columns and Viscous Dampers*, University at Buffalo, The State University of New York, Buffalo, NY, USA, 2007.

[18] H. Roh and A. M. Reinhorn, "Analytical modeling of rocking elements," *Engineering Structures*, vol. 31, no. 5, pp. 1179–1189, 2009.

[19] H. Roh and A. M. Reinhorn, "Nonlinear static analysis of structures with rocking columns," *Journal of Structural Engineering*, vol. 136, no. 5, pp. 532–542, 2010.

[20] H. Roh and A. M. Reinhorn, "Modeling and seismic response of structures with concrete rocking columns and viscous dampers," *Engineering Structures*, vol. 32, no. 8, pp. 2096–2107, 2010.

[21] P. Earthquake Engineering Research Center (Peer), *Report of the Seventh Joint Planning Meeting of NEES/E-Defense Collaborative Research on Earthquake Engineering*, UC Berkeley, Berkeley, CA, USA, 2010.

[22] P. Earthquake Engineering Research Center (Peer), "PEER annual meeting," 2016, https://peer.berkeley.edu/2016-peer-annual-meeting-presentations-website.

[23] X. L. Lv, L. M. Quan, and H. J. Jiang, "Research progress on innovative earthquake-resilient structural systems," *Earthquake Engineering and Engineering Dynamics*, vol. 37, no. 3, pp. 1–9, 2017, in Chinese.

[24] X. L. Lv, *Earthquake Resilient Structures – Basic Concept and Design Methodology*China Building Industry Press, Beijing, China, 2020.

[25] C. X. Mao, Q. Yu, and H. Y. Zhang, "Pseudo-static tests of prestressed self-centering reinforced concrete column and beam-column joints," *Journal of Natural Disasters*, vol. 26, no. 6, pp. 1–12, 2017.

[26] L. Tirca, O. Serban, L. Lin, M. Wang, and N. Lin, "Improving the seismic resilience of existing braced-frame office buildings," *Journal of Structural Engineering*, vol. 142, no. 8, Article ID C4015003, 2016.

[27] G. Pekca, A. M. Itani, and C. Linke, "Enhancing seismic resilience using truss girder frame systems with supplemental

devices," *Journal of Constructional Steel Research*, vol. 94, pp. 23–32, 2014.

[28] M. Pollino, "Seismic design for enhanced building performance using rocking steel braced frames," *Engineering Structures*, vol. 83, pp. 129–139, 2015.

[29] L. L. Song, T. Guo, Y. Gu, and Z. L. Cao, "Experimental study of a self-centering prestressed concrete frame subassembly," *Engineering Structures*, vol. 88, pp. 176–188, 2015.

[30] M. Khanmohammadi and S. Heydari, "Seismic behavior improvement of reinforced concrete shear wall buildings using multiple rocking systems," *Engineering Structures*, vol. 100, pp. 577–589, 2015.

[31] B. Qu, F. Sanchez-Zamora, and M. Pollino, "Mitigation of inter-story drift concentration in multi-story steel concentrically braced frames through implementation of rocking cores," *Engineering Structures*, vol. 70, pp. 208–217, 2014.

[32] Y. Liu, Z. X. Guo, X. Liu, R. Chicchi, and B. Shahrooz, "An innovative resilient rocking column with replaceable steel slit dampers: experimental program on seismic performance," *Engineering Structures*, vol. 183, pp. 830–840, 2019.

[33] X. L. Lv, Y. Cui, and J. J. Liu, "Shaking table test of a self-centering reinforced concrete frame," *Journal of Building Structures*, vol. 35, no. 1, pp. 19–26, 2014.

[34] L. Lu, L. Jiang, and H. Li, "Shaking table tests for aseismic performance of a controllable rocking reinforced concrete frame with column-end-hinge joints," *Journal of Vibration and Shock*, vol. 35, no. 4, pp. 193–198+216, 2016.

[35] C. Jiang, W. J. Gao, and X. L. Lv, *Rocking Component and Numerical Modeling of Rocking Column Based on OpenSEES*Science Paper Online, Beijing, China, 2013.

[36] in*GB 50010-2010, Code for Design of Concrete Structures*National Standard of the People's Republic of China, Beijing, China, 2015.

[37] T. Wang, *Study on Resilient Performance of an Innovate Self-Centering Hybrid Rocking Column*Shenyang Jianzhu University, Shenyang, China, 2022.